50
Satellite Formation-Flying and Rendezvous

Simone D'Amico[1] and J. Russell Carpenter[2]

50.1
Introduction to Relative Navigation

GNSS has come to play an increasingly important role in satellite formation-flying and rendezvous applications. In the last decades, the use of GNSS measurements has provided the primary method for determining the relative position of cooperative satellites in low Earth orbit. More recently, GNSS data have been successfully used to perform formation-flying in highly elliptical orbits with apogees at tens of Earth radii well above the GNSS constellations. Current research aims at distributed precise relative navigation between tens of swarming nano- and micro-satellites based on GNSS.

Similar to terrestrial applications, GNSS relative navigation benefits from a high level of common error cancellation. Furthermore, the integer nature of carrier phase ambiguities can be exploited in carrier phase differential GNSS (CDGNSS). Both aspects enable a substantially higher accuracy in the estimation of the relative motion than can be achieved in single-spacecraft navigation. Following historical remarks and an overview of the state-of-the-art, this chapter addresses the technology and main techniques used for spaceborne relative navigation both for real-time and offline applications. Flight results from missions such as the Space Shuttle, PRISMA, TanDEM-X, and MMS are presented to demonstrate the versatility and broad range of applicability of GNSS relative navigation, from precise baseline determination on-ground (mm-level accuracy), to coarse real-time estimation on-board (m- to cm-level accuracy).

50.1.1
History and State-of-the-Art

Satellite formation-flying and rendezvous demand knowledge of the relative motion between multiple spacecraft to acquire, maintain, and reconfigure a given geometry. For single-satellite navigation, absolute positioning accuracies in the 50–5 cm range can presently be achieved with GNSS depend-

---

1) Stanford University
2) NASA Goddard Space Flight Center

ing on the timeliness requirements (onboard real-time versus ground-based offline processing), the hardware capabilities (single versus multi-frequency receiver) and the sophistication of the processing techniques. On the other hand, the full potential of GNSS can best be exploited in relative navigation, where mm-level positioning accuracies can be achieved through the use of CDGNSS (Figure 50.1).

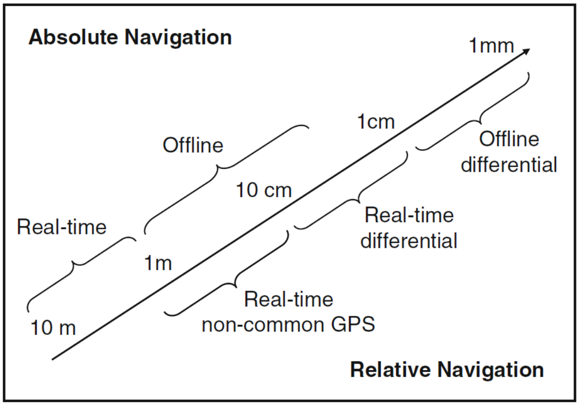

Figure 50.1 Range of achievable GNSS navigation accuracies using absolute and relative positioning techniques [1].

This capability is well known in geodesy but likewise applicable to formation-flying and rendezvous missions in space despite the different signal-tracking and flight dynamics environment. Many formations can be controlled based on absolute orbit determination results for the individual spacecraft, but a relative navigation technique is required for separations of less than a few hundred meter. Although the use of GNSS-based navigation is of primary relevance for missions in low Earth orbits, where one can fully benefit from the simultaneous tracking of numerous GNSS satellites, GNSS-based relative navigation has been recently applied for formation-flying in highly elliptical orbits above the GNSS constellations. Likewise, GNSS relative navigation is considered for formation-flying in cis-lunar space, and for the collocation and servicing of geostationary satellites.

The following subsections review how GNSS-based relative navigation supported a variety of mission types in human history, from rendezvous to formation-flying, both through ground-in-the-loop processing or autonomous on-board implementation.

50.1.1.1 **Rendezvous Missions**

Early studies of the options for achieving a moon landing led NASA to pioneer the techniques and methods for performing orbital rendezvous during the Gemini program in the 1960s. The rendezvous navigation filtering methods developed by NASA for the Apollo missions were carried over to the Space Shuttle[2, 3]. While NASA was finalizing the Space Shuttle design in the late 1970s, GPS Block I was also being deployed, and NASA “scarred” the last three orbiters Discovery, Atlantis, and Endeavour for eventual GPS usage with antennas and associated harnesses. Eventually, NASA fully equipped all the orbiters with GPS in response to a proposed phase-out of the Tactical Air Navigation (TACAN) system, but the Space Shuttle never used GPS operationally for rendezvous[4].

Nonetheless, as the international community developed plans for the International Space Station (ISS) in the 1990s, it became clear that GPS would provide an important capability for autonomous visiting vehicles to perform far-range rendezvous maneuvers prior to target acquisition by proximity sensors. NASA and ESA collaborated to perform a series of relative GPS flight demonstrations[5] as precursors to the deployment of ESA's Automated Transfer Vehicle (ATV): on Shuttle mission STS-69 in September 1995 between Endeavour and a shuttle-deployed free-flyer called Wake Shield Facility[6, 7]; on STS-80 in late 1996 between the orbiter Columbia and a free-flyer called ASTRO-SPaS[8, 9]; and on STS-84 and STS-86 in May and October of 1997, respectively, between Atlantis and the Mir Space Station[10]. During most of these experiments, GPS data were recorded on-board and later processed for ground analysis to demonstrate accuracies at the 10-100 m level using mainly pseudorange measurements. Meanwhile, the National Space Development Agency of Japan (NASDA) was preparing for the H-II Transfer Vehicle (HTV) with the Experiment Test Satellite (ETS) VII mission, which demonstrated closed-loop proximity operations using GPS and other sensors for the first time in 1998 and 1999[11]. The 2.5 ton chaser spacecraft and the 0.4 ton target satellite were each equipped with a 6-channel GPS receiver that offered a pseudorange accuracy of about 7 m and delta range accuracy of 1.5 cm (rms). Based on a filtering of differential pseudoranges and carrier phases a relative position and velocity accuracy of 10 m and 3 cm/s, respectively, was obtained in comparison to a post-processed trajectory. This is well within the specified limits of 21 m and 5 cm/s established for the far-range approach down to a 150 m distance. Further improvements down to 5 m and 1 cm/s were later achieved offline by incorporation of carrier phase measurements[12].

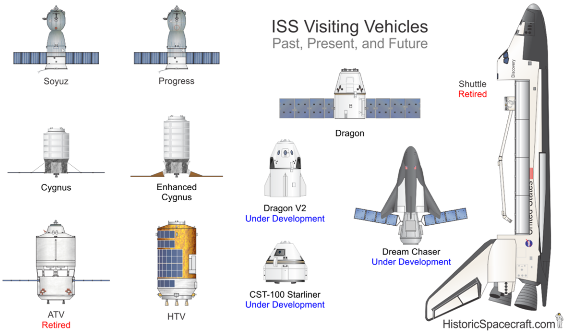

Figure 50.2 International fleet of space vehicles using GPS for far-range navigation relative to the ISS. Credits: HistoricSpacecraft.com.

The GPS rendezvous navigation technologies demonstrated in the 1990s became operational in the 2000s. Notably, the ATV's GPS based real-time relative navigation system (RGPS) is intended for approach navigation in the 30-0.3 km distance range and received its flight qualification on the Jules Verne maiden flight in April 2008. It processes data from the 9-channel Laben Tensor GPS receiver on the ATV and the Russian 12-channel ASN-M receiver onboard the ISS in a relative navigation filter based on the Hill-Clohessy-Wiltshire dynamical model [13]. Besides pseudorange or code phase data, the filter makes use of Doppler or carrier phase measurements to improve the velocity knowledge. Compared to the filtering of GPS receiver positioning fixes, the RGPS module of ATV achieved accuracies in the 10 m and 2 cm/s range[14]. Between 2008 and 2014, five ATV missions resupplied the ISS using RGPS. Similarly, HTV has performed five successful resupply missions to the ISS between 2009 and 2015, with plans for four more through 2019. Starting in 2012 with the SpaceX Dragon, commercial resupply services to the ISS have begun, including also Orbital ATK's Cygnus. As of May 2016, NASA has signed contracts for follow-on commercial cargo and commercial crew services with these companies, as well as Sierra Nevada Corporation and Boeing (Figure 50.2). And NASA's Orion Multi-Purpose Crew Vehicle also plans to use GPS in support of far-range rendezvous navigation in near-Earth regimes[15].

50.1.1.2 **Formation-Flying Technology Demonstration Missions**

The rendezvous activities described in the previous section make use of coarse GNSS relative navigation (m-level accuracy), mainly for far-range operations (kilometers), and are characterized by short mission durations (a few hours or days). The typical objective is to assemble, supply, or maintain a larger structure in space. A second class of space missions that is enabled by GNSS relative navigation is represented by spacecraft formation-flying. Here, two or more vehicles interact remotely to build scientific instruments otherwise very difficult or impossible to realize through a single monolithic platform. In contrast to single spacecraft, formation-flying satellites separated along the orbit allow revisit times ranging from hours to minutes down to milliseconds. A spatial distribution of spacecraft looking at the same ground region or celestial target allows for direct interferometric observations whereby multiple spacecraft act as a single huge virtual instrument in space. Even larger separations between spacecraft allow in-situ synchronous measurements with global coverage of the environment (e.g., atmosphere or magnetosphere). In contrast to satellite rendezvous, satellite formation-flying is typically characterized by longer durations (years) and tighter requirements on GNSS relative navigation accuracy, from decimeter- down to millimeter-level accuracy in relative position knowledge [16].

In view of the recognized potential and tight requirements, a number of demonstration missions have been deployed in the past employing formation-flying technology. In November 2000, NASA launched Earth Observer 1 (EO-1), which used GPS to perform the first series of formation-flying demonstrations with Landsat-7 between January and June of 2001[17]. The EO-1 formation-flying technology requirements were to demonstrate the capability to autonomously fly over the Landsat-7 ground-track within +/-3 km as measured at the equator, and autonomously maintain the formation for extended periods of time to enable paired scene comparisons between the two satellites. After an extensive validation phase of two months, a total of nine maneuvers were finally planned and executed autonomously by EO-1 based on navigation solutions from the on-board GPS receiver and post-processed ground-tracking state information of the companion Landsat-7 satellite.

It took ten years for the first long-term routine demonstration of precise on-board relative navigation based on carrier-phase differential GPS (CPDGPS). This was carried out by the PRISMA formation-flying mission (Sweden, Germany, France) during a time-frame of about five years from its launch in June 15, 2010 from Yasny, Russia [18, 19]. The GPS relative navigation system employs DLR's single-frequency 12-channels Phoenix receivers, a dual-inertial Extended Kalman Filter (EKF) which processes GRoup And Phase Ionospheric Correction (GRAPHIC) data-types and single-difference carrier-phase measurements as the primary formation-flying sensor on-board the PRISMA satellites [20]. Its key objective is the continuous provision of accurate and reliable relative position and velocity information at all times during the mission. The relative navigation state is used on-board the active Mango spacecraft to autonomously control its motion with respect to the passive Tango throughout a multitude of experiment scenarios including, among others, formation keeping and reconfiguration of passive relative orbits and quasi-continuous control of forced motion trajectories. In the absence of a relative navigation system characterized by higher technology readiness level, relative GPS represents also the safe mode sensor of the PRISMA formation. In particular, the GPS relative navigation is used on-board Mango to support fault detection isolation and recovery (FDIR) functionalities like relative motion monitoring and collision avoidance. The twofold scope of the GPS navigation onboard PRISMA poses challenging requirements to the system design since ultimate accuracy is desired for precision control purposes whereas robustness and reliability are needed for safe mode activities[18]. The PRISMA satellites were released, clamped together in launch configuration, into a nominal dusk-dawn orbit at a mean altitude of 757 km, 0.004 eccentricity and 98.28 deg inclination. After the successful accomplishment of the launch and early operations phase, on June 17, 2010, PRISMA entered a 57-days long commissioning phase. This phase was characterized by the careful verification and checkout of on-board equipment, essential on-board functions and by the calibration of navigation algorithms such as attitude, rate estimators, and GPS-based navigation. Most of the commissioning phase operated PRISMA as a combined spacecraft where Tango was still mated to Mango. However, the last part of this phase included the Tango separation from Mango (on August 11, 2010) and the subsequent GPS relative navigation calibration campaign (5 days from August 16, 2010). The flight results from the initial and final commissioning phase of the GPS navigation system have been presented in [21, 22]. The successful completion of the commissioning phase and a consolidation of the real-time navigation filter parameters paved the way to the start of the nominal PRISMA mission. Five years of primary and secondary experiments have been successfully conducted virtually without interruptions (Figure 50.3). The GPS-based relative navigation has been demonstrated to properly perform under all possible formation-flying scenarios within the range of the UHF-band inter-satellite link, i.e., between approximately 1 m (in clamped configuration) and 50 km (maximum separation achieved in the nominal mission). Key flight results from the PRISMA GPS-based navigation system obtained during the conduction of various experiments have been presented in [23, 24]. In most of the encountered scenarios, the demonstrated overall performance is below 10 cm and 1 mm/s (3D, rms) for relative position and velocity respectively as cross-compared with precise GPS orbit products on-ground and other metrology systems employed on the PRISMA mission (radio-frequency and vision-based) [25]. The navigation error budget is dominated by maneuver executions, attitude estimation errors, multi-path, and antenna phase pattern distortions.

Figure 50.3 Graphical illustration of PRISMA technology demonstration mission (left). Images of the PRISMA's Tango spacecraft captured by the Mango close-range navigation camera during close-proximity operations at 10 m distance based on CPDGPS (right) [25]. Credits: OHB Sweden.

Close to the end of the PRISMA mission in November 2014, the Canadian CanX-4 and CanX-5 nanosatellites demonstrated autonomous dual-spacecraft formation-flying based on CPDGPS in low Earth orbit at a scale never accomplished before [26]. In comparison with the PRISMA satellites which weight 145 kg (Mango) and 50 kg (Tango), the CanX spacecraft is approximately 6 kg with associated costs which are one of order magnitude smaller than PRISMA. Launched on June 30, 2014 from Sriharikota, India, CanX-4 and CanX-5 were deployed separately following launch, after which a series of ground-based drift recovery maneuvers were executed to bring the spacecraft within communication range of each other. Subsequently, the spacecraft used on-board propulsion, an S-band inter-satellite link, and relative navigation based on CPDGPS techniques to perform series of precise, controlled, autonomous formations from 1 km range down to 50 m separation. The relative navigation algorithm is an EKF which uses single-difference carrier-phase measurements to estimate the relative state of the deputy with respect to the chief as an input to the formation control laws. In the absence of an external and independent metrology system, it is difficult to evaluate the obtained accuracy of the relative navigation system. However, measurement residuals and formal state covariance are compatible with decimeter-level relative positioning errors, especially when a large number of commonly visible GPS satellites (up to 14) is in view of the formation-flying nanosatellites [26].

50.1.1.3 **Formation-Flying Science Missions**

In parallel with the aforementioned technology demonstrations, three groundbreaking science missions have adopted GPS-based formation-flying technology in the past, namely the NASA/DLR's Gravity Recovery and Climate Experiment (GRACE)[27, 28], the DLR's TerraSAR-X Add-on for Digital Elevation Measurement (TanDEM-X)[29, 30], and the NASA's Magnetospheric Multi-Scale (MMS) mission[31, 32], setting the stage for more to come. The GPS relative navigation aspects of each of these mission are summarized in the following.

GRACE is a joint project between NASA and DLR. Initially proposed by the University of Texas at Austin, Center for Space Research (UTCSR), the German Research Centre for Geosciences (GFZ) in Potsdam and the Jet Propulsion Laboratories (JPL) in Pasadena, the twin GRACE satellites were launched from Plesetsk, Russia, on March 17, 2002. Both satellites were placed in the same nominal circular orbit of about 490 km altitude at an inclination of 89 deg. Following Launch and Early Orbit Phase (LEOP) operations, the orbits of the two satellites evolve naturally for the remainder of the mission. During the science data collection, the two GRACE satellites point their K-band feed horns towards each other to a high precision making their states dynamically coupled. Over the mission lifetime the two satellites remain in nearly coplanar orbits. Due to differential drag force, the along-track separation varies, and station-keeping maneuvers are required to keep the two satellites within 170–270 km of each other. The primary objective of GRACE is to obtain accurate global models for the mean and time variable components of the Earth's gravity field. The primary product of the GRACE mission is a new model of the Earth's gravity field every 15–30 days. This is achieved by measuring the distance variations between the satellites using the K-band microwave tracking system with 10 microns precision. In addition, each satellite carries a geodetic quality dual-frequency GPS receiver and a high accuracy accelerometer to enable accurate orbit determination, spatial registration of gravity data, and the estimation of gravity field models. The Earth gravity field estimates obtained from data gathered by the GRACE mission provides, with unprecedented accuracy, integral constraints on the global mass distribution and its temporal variations within the Earth system.

Indeed, the feasibility of precise millimetric baseline reconstruction based on GPS measurements has first been demonstrated within the GRACE mission. As part of the mission operations, orbits of each individual satellite are determined on a routine basis by JPL with an estimated accuracy of a few centimeters. While these exhibit a certain level of common modes, the relative position obtained from a differencing of the absolute trajectories still exhibits representative errors of 10–20 mm (1 σ) in comparison to the high precision K-band measurements of the inter-satellite distance [33]. Early efforts for a fully differential orbit determination exploiting the integer nature of carrier phase ambiguities through double-differenced data types resulted in baseline estimates with precision of several mm in along-track direction and an even better performance of <1 mm was later achieved by researchers at TU Delft, JPL, and the University of Bern [34, 35, 36]. Due to the large separation of the GRACE satellites, ionospheric path delays do not cancel and a rigorous resolution of the L1 and L2 ambiguities is therefore required to achieve relative navigation solutions of this quality. Success rates of about 85% have been documented in the dual-frequency ambiguity resolution [33, 34].

Even though the GRACE mission itself never required a precise relative navigation it paved the way for other missions that rely on GPS-based baseline products of utmost accuracy. The most stringent accuracy requirements in this context have so far been formulated for Synthetic Aperture Radar (SAR) interferometry missions such as the dual-spacecraft TanDEM-X. TanDEM-X was successfully launched in June 2010 in a dusk-dawn sun-synchronous low Earth orbit (97.44 deg, 514 km altitude, frozen eccentricity) with a 167 orbits or 11-day repeat cycle. Since December 2010 the two satellites are orbiting at typical cross-track baselines between 200 m and 400 m. It comprises two formation-flying satellites, each equipped with a SAR to map the Earth's surface with high spatial resolution. Together, the two satellites form a unique single-pass SAR interferometer, offering the opportunity for flexible baseline selection, depending on the terrain under observation. Primary objective of TanDEM-X is the acquisition of a global digital elevation model (DEM) with unprecedented accuracy and resolution (12 m horizontal and 2 m vertical resolution) using cross-track interferometry [29]. Here, complex-valued SAR images are simultaneously taken by two spacecraft and combined into an interferogram from which the terrain height can be derived. In this process, the line-of-sight component of the relative position (or "interferometric baseline") of the two SAR antennas must be known with utmost accuracy. At an X-band wavelength of only 3 cm and a representative SAR incidence angle of about 30 deg, a line-of-sight baseline error of 1 mm will result in vertical and horizontal DEM shifts of 1 and 2 m, respectively [37]. The TanDEM-X project builds directly on experience gained from the GRACE GPS data processing. The two spacecraft of the TerraSAR-X/TanDEM-X formation are equipped with high-grade dual-frequency GPS receivers contributed by the GeoForschungszentrum (GFZ). The Integrated GPS Occultation Receiver (IGOR) selected for the mission represents a commercial rebuild of the BlackJack receiver flown earlier on numerous other science missions. On the TerraSAR-X and TanDEM-X satellites it provides pseudorange and carrier phase measurements with a mean noise level of 15 cm and 0.7 mm, or, equivalently, 21 cm and 1 mm for the receiver-receiver single-difference [38]. Aside from precise orbit and baseline determination, the GPS receivers are also used as radio science instruments for atmospheric sounding. Such radio-occultation measurements of GPS satellites close to the Earth's limb enable the reconstruction of temperature and density profiles of the troposphere and are a key input for global weather models.

As part of the TanDEM-X mission requirements, a 1 mm (1D rms) baseline accuracy has been specified to avoid tilts and shifts in individual DEMs and to enable a flawless mosaicking. In view of the criticality of accurate baseline products for the overall mission performance, the baseline generation is routinely performed by two processing centers at GFZ and the German Space Operations

Center (DLR/GSOC). The two solutions are generated with different algorithms and tool chains to ensure maximum independence and to facilitate a basic consistency check. Furthermore, a merged baseline product is generated from a weighted average of the individual solutions, which is then employed in the DEM generation [38]. A comparison of TanDEM-X baseline products generated by various agencies has been presented in Ref. [39]. Here, differences with a standard deviation of 0.5–1.0 mm per axis have been obtained between individual solutions, but systematic biases of similar size could likewise be identified. These biases reflect the impact of different processing concepts and are of similar order as the biases observed earlier in the GRACE mission. Beyond biases in the GPS-derived relative motion of the two spacecraft, the interferometric SAR processing is likewise affected by uncertainties in the SAR antenna phase centers and instrumental delays. To assess the cumulative impact of all system specific biases on the measured instrument phase, dedicated calibration data takes are performed on a routine basis in the TanDEM-X mission over flat target sites with well known altitude profiles. By comparison with uncalibrated raw DEMs from the SAR interferometry, systematic biases may be identified and corrected. Initial tests documented in Ref. [36] suggest residual biases at the level of a few mm, which is well within the pre-mission expectations. However, a combined analysis of calibration data-takes in different observations modes is required to arrive at a consolidated system calibration [1].

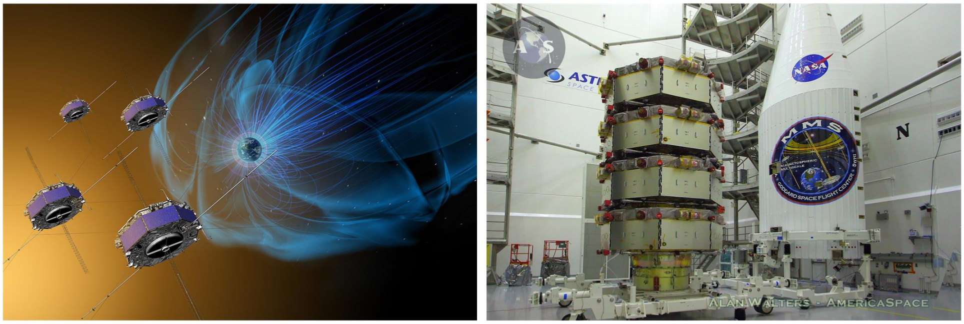

Figure 50.4 Graphical illustration of MMS formation-flying mission in high elliptical orbit (left). All four of MMS spacecraft in the clean room at Astrotech Space Operations in Titusville, Fla., completed and stacked for launch atop a ULA Atlas-V rocket (right). Credits: Alan Walters / AmericaSpace. http://www.americaspace.com.

Besides the precise baseline reconstruction requirements, TanDEM-X is characterized by very challenging and unique formation-flying control requirements to be met through GPS. The TerraSAR-X osculating orbit is maintained within a maximum absolute cross-track distance of 250 m from a target Earth-fixed reference trajectory, which is comprised of exactly matching states at beginning and end of the 11-day cycle enabling highly repeatable data-take conditions [40]. Absolute orbit control maneuvers to counteract luni-solar perturbations and to compensate atmospheric drag are performed 3–5 times per year (out-of-plane) and up to 3 times per week (in-plane) during periods of high solar activity, respectively[41]. These maneuvers are replicated identically by both spacecraft, on the other hand formation acquisition and maintenance maneuvers are exclusively performed by the TanDEM-X satellite. Because of the near-circular low Earth orbit and the mutual distance on the order of 1 km, linearized equations can be used to describe the relative motion. The model employs relative orbital elements as state parameters to improve linearization accuracy at large separations and accounts for J2 and differential drag perturbations[42]. The use of the relative eccentricity/inclination vector separation method for formation design enables safe proximity operations and a flexible adjustment of the interferometric baseline [43]. For the purpose of relative navigation within the ground-based flight dynamics system, the filtering of GPS navigation solution data is preferred to the processing of raw pseudorange and/or carrier phase data. As a consequence, the amount of auxiliary information is significantly reduced leading to higher robustness with sufficient relative orbit determination accuracy of typically <0.5 m in cross-track (2D, rms) and <1 m (rms) in along-track direction [44]. In addition, the mission features the TanDEM-X Autonomous Formation Flying System (TAFF) for autonomous formation keeping during along-track SAR interferometry campaigns where higher control accuracy is required[43]. TAFF is a software extension of the TanDEM-X Attitude and Orbit Control System (AOCS) which makes use of EADS/Astrium's Mosaic single-frequency GPS receivers embarked on both spacecraft, an S-band inter-satellite link, and two pairs of 40 mN cold gas thrusters on TanDEM-X. TAFF processes GPS navigation solutions as measurements and an EKF to estimate relative orbit elements for in-plane formation keeping. Early flight results demonstrate sub-meter relative navigation accuracy and m-level formation control accuracy in radial and along-track directions[45].

The highest-altitude operational usage of GPS to date has been accomplished in the frame of the Magnetospheric Multi-Scale (MMS) mission. Launched in March of 2015, MMS consists of a controlled formation of four spin-stabilized spacecraft in similar highly elliptic orbits reaching apogee at radial distances of 12 and 25 Earth radii (RE) in the first and second phases of the mission and up to 60 RE in the extended mission phase. MMS investigates how the Sun's and Earth's magnetic fields connect and disconnect, explosively transferring energy from one to the other in a process that is important at the Sun, other planets, and everywhere in the universe, known as magnetic reconnection. The science goal of MMS is to reveal, for the first time, the small-scale three-dimensional structure and dynamics of the elusively thin and fast-moving electron diffusion region. This is done through four identically instrumented MMS spacecraft which fly in an adjustable pyramid-like formation. Navigation for MMS is achieved independently on-board each spacecraft by processing GPS observables using NASA Goddard Space Flight Center (GSFC)'s Navigator GPS receiver and the Goddard Enhanced Onboard Navigation System (GEONS) EKF software. GEONS is a high-heritage software package developed at GSFC for on-board orbit determination. It implements a UD-factorized EKF with a fourth or eighth order fixed-step Runge-Kutta integrator and realistic process noise models. For MMS, GEONS is configured to estimate absolute position and velocity vectors, clock bias, rate, and acceleration. The integrator is configured with a 10 second step size. The dynamics model uses a 13×13 geopotential, solar and lunar point masses, solar radiation pressure with spherical area model, and atmospheric drag. It processes L1 C/A undifferenced pseudorange observables provided by the Navigator GPS receiver at a 30 s interval. Accelerometer data is provided from the attitude control system at a 10 s interval during maneuvers.

Flight data show that the MMS GPS receiver is able to track, on average, more than eight signals in the region above the GPS constellation and, at times, even 12 signals at the 12 RE apogee. At 25 RE apogee, Navigator continues to track 4-6 satellites, which is the highest apogee yet achieved by the mission. It is noted that apogee raising up to 28 RE is planned to occur in the extended mission phase, and an eventual raise to 60 RE is under consideration. Reference [32] describes results from a certification campaign that occurred during the first nine weeks of the MMS mission. During this period, the GSFC Flight Dynamics Facility (FDF) performed daily ground-based orbit determination solutions based on two-way range and Doppler tracking from Tracking and Data Relay Satellite

System in the vicinity of MMS perigees, and near-continuous two-way Doppler tracking from the Deep Space Network throughout the remainder of the MMS orbits. The highlight of the certification campaign was a three-day window from day 133 through 136 of 2015, when all other spacecraft commissioning activities ceased, so as to provide a quiescent window for orbit determination calibration. The FDF used definitive attitude products and communications antennas center-of-mass offsets to remove the signature of the MMS spacecrafts' spin rate from the tracking data. The FDF then processed these "de-spun" data using the filter-smoother in Orbit Determination Toolkit from Analytical Graphics, Inc. to provide an independent radiometric reference solution. Comparison between these solutions and the on-board solution implied that GEONS was achieving position accuracies of better than 50 m, and semi-major axis accuracies of better than 5 m. Comparison of the formal covariances from the ground-based and on-board solutions suggest that the majority of the differences between the two solutions is attributable to the ground-based solutions.

50.1.2
Potential and Future Applications

The success of the technology demonstration and scientific projects described in the previous sections has motivated the definition of even more advanced space missions which rely on GPS relative navigation to achieve their objectives. Relevant examples are given by the NASA's GRACE follow-on (GRACE-FO) [46], the DLR's TanDEM-L [47], and the ESA's PROBA3 [48] formation-flying missions. GRACE-FO and TanDEM-L represent incremental advances based on their predecessors, further enhancing the capability to recover the dynamics of the Earth's internal and surface processes with increased quality and resolution. Due to launch in late 2020, PROBA-3 is the third mission in ESA's Project for Onboard Autonomy. PROBA-3 will demonstrate precision formation-flying using optical metrology and pave the way for future astronomical formation-flying missions based on virtual telescopes or distributed apertures. PROBA-3 itself will enable observation of the solar corona with one spacecraft acting as occulter and one spacecraft carrying the instrumentation. The relative position and attitude of the two spacecraft will be tightly controlled to form a virtual telescope with a length of 150 m. The two spacecraft will be launched into a highly elliptical orbit with a period of about 20 hours and a 59 deg inclination. Along this orbit, the altitude varies from 800 km to more than 60,000 km. The high apogee altitude enables long arcs of fine formation keeping and coronagraph operations due to the very low level of orbital perturbations. In total, science operations will be performed throughout a six-hour-arc centered on apogee during which the formation is controlled by high-accuracy lateral laser metrology and micro-Newton thrusters. After the apogee, the formation is broken up and later reassembled in a sequence of mid-course and fine correction maneuvers [49]. Both the Occulter and Coronagraph spacecraft will be equipped with a cold-redundant pair of GPS receivers. Due to the limitations in GPS visibility at high altitudes, the receivers will primarily be operated in the vicinity of the perigee passages. Despite a limited orbital coverage, the GPS measurements will enable the determination and prediction of the spacecraft orbit with adequate accuracy for mission planning and operations (e.g., antenna pointing, scheduling). More importantly, relative navigation information from the GPS tracking on both spacecraft will be used to assist the autonomous planning of the mid-course maneuvers and the reacquisition of the formation after the perigee passage. In view of tight financial and engineering budgets, the use of commercial-off-the-shelf (COTS) GPS technology is considered as a baseline for the PROBA-3 mission. Other than receivers specifically designed for use in highly elliptical orbit or geostationary orbit, COTS receivers will primarily be able to track GPS signals and provide a navigation fix in the vicinity of the pericenter arc. Navigation information at other points of the orbit will be generated through orbit prediction after adequate filtering of the GPS measurements collected during the perigee passage. For the PROBA-3 mission, an investigation has been carried out into the possibility of using GPS-based relative navigation to aid in formation re-acquisition after perigee transits, or possibly even employing GPS as the primary navigation sensor for formation re-acquisition [50]. In this case, the navigation and control performance of the GPS-based formation acquisition system shall allow the transition to optical metrology at apogee, i.e. the achieved relative position at apogee shall be compliant with the maximal utilization range of the optical metrology system (250 m). Realistic hardware-in-the-loop simulations [50] show that the PRISMA GPS relative navigation system can be used to perform relative navigation with cm-level accuracy during the perigee phase. Afterwards, the orbit prediction performance depends mainly on the quality of the onboard modeling of the differential solar radiation pressure acting on the satellites. When not taken into account, this perturbation is responsible for relative navigation errors at apogee up to 50 m. The errors can be reduced to only 10 m if the navigation filter is able to model this disturbance with 70% fidelity. Overall, the study demonstrates the feasibility and the good relative navigation performance of a GPS-based relative navigation system for formation acquisition and coarse formation keeping in high elliptical orbits.

On the technology demonstration front, the Cubesat Proximity Operations Demonstration (CPOD) will demonstrate rendezvous, proximity operations and docking (RPOD) using two 3-unit (3U) CubeSats weighing approximately 5 kg. This flight demonstration will validate and characterize new miniature low-power proximity operations technologies applicable to future missions. The two CPOD satellites are scheduled to be launched together in low Earth orbit in late 2017. CPOD will demonstrate the ability of the two nanosatellites to do formation keeping, reconfiguration, circumnavigation, and docking. Many of the proximity operations test scenarios will be performed autonomously using high-performance on-board processors and flight software for guidance, navigation and control. The two CPOD satellites will be deployed into orbit simultaneously while attached side-by-side and will initially undergo a series of checkout steps to ensure proper operation and maneuvering capability. Once the initial checkout is complete, the two spacecraft will then release from each other and will begin the proximity operations maneuvers. The space-to-ground data link from each satellite will enable transmission of images of the other satellite. The two spacecraft will use an inter-satellite link to share GPS navigation solutions and other auxiliary data. Using on-board navigation systems, one satellite will perform a series of circumnavigation maneuvers relative to the second satellite in order to validate and characterize performance of the new miniature sensors. After the sensors have been characterized, the chaser satellite will begin closing the distance to the first satellite during a series of planned maneuvers. Finally, when they have reached a close relative range, they will conduct the last portion of the mission by engaging the docking mechanism and performing a full docking of the two spacecraft. This mission opens a new frontier for exploration and operations with small spacecraft. In addition, the CPOD mission enhances the capability of small spacecraft to work in coordination with one another for observations or to become building blocks for more sophisticated space systems. The CPOD project is led by Tyvak Nano-Satellite Systems Inc. of Irvine, California. The company has partnered with Applied Defense Solutions Inc. of Columbia, Maryland, and the California Polytechnic State University of San Luis Obispo, California. The CPOD mission is funded through NASA's Small Spacecraft Technology Program (SSTP), which is chartered to develop and mature technologies to enhance and expand the capabilities of small spacecraft with a particular focus on communications, propulsion, pointing, power and autonomous operations. For more information on CPOD the reader is referred to [51].

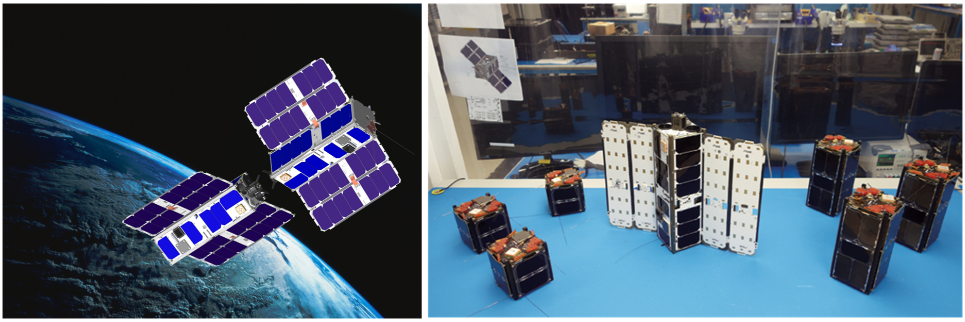

Figure 50.5 Graphical illustration of CPOD (left), https://www.nasa.gov. Tyvak's nanosatellite fleet, including CPOD engineering model (right), http://satmilmagazine.com. Credits: Tyvak Nano-Satellite Systems Inc.

As a natural evolution of CPOD, NASA's SSTP is funding the Distributed multi-GNSS Timing and Localization (DiGiTaL) system under development by the Stanford's Space Rendezvous Laboratory (SLAB), in collaboration with NASA's GSFC and Tyvak [52]. The goal of DiGiTaL is to provide nanosatellite formations with unprecedented, centimeter-level relative navigation accuracy in real-time and nanosecond-level time synchronization. This is achieved through the integration of a multi-GNSS receiver (Novatel OEM628), a Chip-Scale Atomic Clock (CSAC) by Jackson Labs Technologies, Inc., a UHF inter-satellite link and on-board microprocessor for a total 0.5U volume CubeSat payload. To meet the strict requirements of future miniaturized distributed space systems, DiGiTaL uses error-cancelling combinations of raw carrier-phase measurements which are exchanged between the swarming nanosatellites through a decentralized network. A reduced-dynamics estimation architecture on-board each individual nanosatellite processes the resulting millimeter-level noise measurements to reconstruct the full formation state with high accuracy. Although carrier-phase measurements offer millimeter-level noise, they are subject to an integer ambiguity, which is an unknown integer number of cycles. These ambiguities must be resolved in real-time on-board the spacecraft to meet the accurate relative positioning goals of this project. As this is a very computationally intensive task, it is often beyond the capability of spaceborne microprocessors. In contrast to standard offline approaches, DiGiTaL leverages diverse combinations of measurements from new GNSS signals and frequencies, including GPS, Galileo and Beidou navigation satellite systems. This enables the creation of wide-lane data types to efficiently resolve integer ambiguities. The estimation architecture is embedded in a distributed network of nanosatellites and is intended to support all operational scenarios, while coping with data handling and communication constraints. To this end, each DiGiTaL instance processes measurements from only a limited number of satellites simultaneously. The resulting estimates produced by each nanosatellite are then combined in a dedicated swarm orbit determination algorithm to provide full formation orbit knowledge. Contingency scenarios are aided by a near-omnidirectional antenna system (Tallysman TW-3972E) and a CSAC, which supports accurate orbit propagation and faster convergence times in GNSS-impaired scenarios. DiGiTaL is motivated by two key technologies which are revolutionizing the way humans conduct spaceflight: the miniaturization of satellites and the distribution of payload tasks among multiple coordinated units. The combination of these techniques is leading to a new generation of space architectures, so-called distributed space systems which promise breakthroughs in space, planetary and earth science, as well as on-orbit servicing, and space situational awareness. Some specific mission applications of DiGiTaL include, but are not limited to, synthetic aperture radar interferometers, differential gravimeters, starshade/telescope systems for the direct imaging of the star vicinity, and autonomous assembly of larger structures in space.

50.2
Relative Orbit Determination

The estimation of the relative motion between spacecraft in formations, swarms, rendezvous, or distributed space systems in general, is often referred to as relative orbit determination. This is to distinguish it from absolute orbit determination, which is typically the estimation of the motion of a single spacecraft with respect to the center of mass of a primary attractive body (e.g., the Earth). The combination of a dynamics model for the state of interest and a GNSS measurement model enables a prediction of the measurements for a given set of initial conditions and model parameters. By comparing the difference of the actual observation and the modeled measurements, corrections to the assumed parameters may be inferred to obtain an optimal estimate of the spacecraft state and related parameters. Relative orbit determination approaches developed in the past differ in the choice of state parameters, dynamics model, adopted measurements, and filtering schemes. There is no unique choice that can be recommended for all types of applications and a trade-off between accuracy, robustness and computational load will have to be made in each individual case to meet the given mission requirements. Since many of the techniques used in relative orbit determination are described elsewhere in this book, primarily Chapter 49 (absolute orbit determination) and 35 (differential observables), this Chapter focuses on unique aspects that characterizes relative orbit determination. These topics include state representations and corresponding dynamical models for relative orbits, state predictability, uncertainty considerations, and estimation algorithms suited to real-time embedded systems or on-ground post-processing applications.

50.2.1
State Representations and Dynamics Models

Different sets of estimation parameters have been considered in relative orbit determination by several authors and the following discussion aims to highlight a few aspects of general interest. Fundamentally, the filter may comprise the following types of parameters: 1) spacecraft motion described by position/velocity or orbit elements; 2) dynamics model parameters such as atmospheric/solar radiation pressure coefficients, maneuver delta-v, and empirical accelerations; 3) measurement model parameters such as receivers' clock-offsets, carrier-phase ambiguities, receivers' channel-wise (dual-frequency) or common vertical (single-frequency) ionospheric path delays. Most of these parameters can either be handled as absolute quantities (i.e., referring to a single spacecraft) or relative quantities (i.e., describing the difference of a parameter for one satellite relative to a reference spacecraft in the formation) and both representations can be rigorously transformed into each other. For example, "relative-only" filters have been proposed in [53, 54, 33], while a fully symmetric handling using absolute state vectors for all spacecraft in the formation has been adopted in [55, 56, 35], to name a few. Irrespective of the approach, a relative state, $\Delta \boldsymbol{x}$, can always be obtained by combining the absolute states of individual spacecraft, $\boldsymbol{x}_1$ and $\boldsymbol{x}_2$, through

$$\Delta \boldsymbol{x} = \boldsymbol{x}_2 - \boldsymbol{x}_1 \tag{50.1}$$

and its covariance can be computed from

$$\begin{gathered} \boldsymbol{P}_{\text{rel}} = \mathrm{E}\big[\boldsymbol{e}(\Delta \boldsymbol{x})\boldsymbol{e}(\Delta \boldsymbol{x})^T\big] \\ = \mathrm{E}\big[\boldsymbol{e}(\boldsymbol{x}_1)\boldsymbol{e}(\boldsymbol{x}_1)^T\big] + \mathrm{E}\big[\boldsymbol{e}(\boldsymbol{x}_2)\boldsymbol{e}(\boldsymbol{x}_2)^T\big] - \mathrm{E}\big[\boldsymbol{e}(\boldsymbol{x}_1)\boldsymbol{e}(\boldsymbol{x}_2)^T\big] - \mathrm{E}\big[\boldsymbol{e}(\boldsymbol{x}_2)\boldsymbol{e}(\boldsymbol{x}_1)^T\big] \\ = \boldsymbol{P}_1 + \boldsymbol{P}_2 - \boldsymbol{P}_{12} - \boldsymbol{P}_{12}^T \end{gathered} \tag{50.2}$$

where $\boldsymbol{e}$ denotes the estimation error for the quantity in argument and E denotes the expectation operator. In many applications, the only navigation sensor is a GNSS receiver and there is no method for exchanging synchronous GNSS data between the spacecraft. This is the case for constellations or large satellite formations such as the aforementioned EO-1 and MMS missions. Assuming that errors in the GNSS constellation data are minimal, each satellite's measurement errors will be largely uncorrelated. Furthermore, there may be no common sources of dynamical error, such as might arise from common yet imperfect models of atmospheric density for low Earth orbiters. In such cases, the cross-covariance between state estimates vanishes, $\boldsymbol{P}_{12} = \mathbf{0}$, and mission requirements may be met by performing independent state estimation on-board each satellite, and differencing the estimated state vectors. Since the covariance is positive definite and the covariance of the relative state is given by the sum of the covariance of the absolute states, from Eq. 50.2, the relative navigation errors will always be larger than the absolute navigation error. For applications with tighter mission requirements, it is possible to exploit the cross-covariance of individual states to reduce the relative navigation error. Such a correlation structure can be introduced either through a relative dynamics model or through differential measurements or both. This is the approach used in the on-board navigation systems of missions such as TanDEM-X and PRISMA (see previous paragraph).

The dynamics of the relative motion can be defined in terms of relative position and velocity (using curvilinear or rectilinear coordinates) in the Hill coordinate frame [57]. Its origin is found at the reference spacecraft or chief's center of mass (also called radial/along-track/cross-track, RTN, or local-vertical-local-horizontal, LVLH, frame), in terms of combinations (linear or nonlinear) of orbital elements of the chief and deputy, or through alternative representations based on integration constants, canonical epicyclic elements, or quaternion-based, to name the most common. A comprehensive survey of state representations for relative dynamics is provided in Ref. [58]. Besides the geometric interpretation of these variables, the most important difference is given by the differential equations of relative motion resulting from the use of different state representations[59]. Using non-dimensional Hill's (or RTN) coordinates, $\delta \boldsymbol{x} = (\delta \boldsymbol{r}, \delta \boldsymbol{v})^T$, with relative position $\delta \boldsymbol{r} = (x, y, z)^T$, relative velocity $\delta \boldsymbol{v} = (x', y', z')^T$, and the chief's true anomaly f_c as independent variable, the nonlinear equations of relative motion have the following form[59]

$$\begin{aligned} x'' - 2y' &= \frac{\partial W}{\partial x} + d_x \\ y'' + 2x' &= \frac{\partial W}{\partial y} + d_y \\ z'' &= \frac{\partial W}{\partial z} + d_z \end{aligned} \tag{50.3}$$

where the pseudo-potential $W = W(\delta\boldsymbol{r}, f_c, e_c)$ is a scalar function of the relative position, true anomaly, and eccentricity of the chief, whereas $\boldsymbol{d} = \boldsymbol{d}_d - \boldsymbol{d}_c = (d_x, d_y, d_z)^T$ represent the normalized differential disturbance and control force expressed in the chief's RTN frame. Using combinations of non-dimensional orbit elements, also called Relative Orbit Elements (ROE), $\delta\boldsymbol{\alpha} = \delta\boldsymbol{\alpha}(\boldsymbol{\alpha}_c, \boldsymbol{\alpha}_d)$, the equations of relative motion can be derived through the Gauss Variational Equations (GVE) expressed in matrix form and applied to each individual satellite as [60]

$$\delta\boldsymbol{\alpha}' = \frac{\partial\delta\boldsymbol{\alpha}}{\partial\boldsymbol{\alpha}_c}\boldsymbol{\alpha}'_c + \frac{\partial\delta\boldsymbol{\alpha}}{\partial\boldsymbol{\alpha}_d}\boldsymbol{\alpha}'_d = \frac{\partial\delta\boldsymbol{\alpha}}{\partial\boldsymbol{\alpha}_c}\boldsymbol{G}(\boldsymbol{\alpha}_c)\boldsymbol{d}_c + \frac{\partial\delta\boldsymbol{\alpha}}{\partial\boldsymbol{\alpha}_d}\boldsymbol{G}(\boldsymbol{\alpha}_d)\boldsymbol{R}_{cd}(\boldsymbol{\alpha}_c, \boldsymbol{\alpha}_d)\boldsymbol{d}_d \tag{50.4}$$

where the subscripts c and d indicate quantities referring to the chief and deputy spacecraft respectively, the GVE matrix $\boldsymbol{G}$ has dimension (6x3), and the matrix $\boldsymbol{R}_{cd}$ of dimension (3x3) is introduced to rotate vectors from the chief's to the deputy's RTN frame. All matrices are functions of the osculating orbit elements in argument. The most appropriate definition of relative orbit elements $\delta\boldsymbol{\alpha}$ to be used in Eq. 50.4 depends on the orbit scenario under consideration. It is noted that Eqs. 50.3 and 50.4 are perfectly equivalent to the differential equations of absolute motion of individual spacecraft and hold for elliptic orbits of arbitrary eccentricity. The homogeneous unperturbed solution of Eq. 50.4 (i.e., when $\boldsymbol{d}_d = \boldsymbol{d}_c = \boldsymbol{0}$) is the trivial solution of the Keplerian two-body problem, $\delta\boldsymbol{\alpha} = const$, whereas no unperturbed solution of Eq. 50.3 is available in strictly Hill's coordinates. In the presence of perturbations, as intuition suggests, a state based on ROE is slowly varying with time (or true anomaly) with respect to the orbit period, whereas Hill's coordinates are rapidly varying. Although the dynamics model for relative orbit determination can be based on the numerical integration of Eqs. 50.3 or 50.4, yielding identical results, the GVE-based approach allows the usage of longer integration times for improved computational efficiency in orbit propagation [58]. For missions which call for utmost fidelity (typically cm- or mm-level accuracy), the numerical integration of the equations of motion is required to exploit the millimeter-level noise of carrier-phase measurements. In this case, accurate models for the geopotential, atmospheric drag, solar radiation pressure, and third body forces are used to compute the absolute, $\boldsymbol{d}_d, \boldsymbol{d}_c$ or differential forces $\boldsymbol{d}$ acting on the formation. It is noted that Eqs. 50.3 or 50.4 need to be complemented by the equations of motion of the chief spacecraft. For missions with more benign navigation requirements (dm- or m-level accuracy), semi-analytical or linear dynamics approaches can be used. In particular, ROE are affected by secular, long-period, and short-period effects that can be decoupled in a way similar to what is done for the absolute orbit motion in semi-analytical and general perturbation theories used in well diffused satellite orbital motion propagators such as the Draper Semi-analytical Satellite Theory or the Simplified General Perturbations theory [61]. In addition, short-period variations of the absolute orbit elements, $(\boldsymbol{\alpha}_c, \boldsymbol{\alpha}_d)$ are a function of the location of the spacecraft along the reference trajectory and can often be neglected for navigation and control when differenced to form ROE in $\delta\boldsymbol{\alpha} = \delta\boldsymbol{\alpha}(\boldsymbol{\alpha}_c, \boldsymbol{\alpha}_d)$ [42]. The need to design computationally efficient navigation systems for formation-flying and rendezvous has motivated many authors to linearize Eqs. 50.3 and 50.4 for small nondimensional state parameters. In particular, the linearization of Eq. 50.3 leads to the Tschauner-Hempel equations [62] for arbitrary eccentricity and to the Hill-Clohessy-Wiltshire equations for near-circular orbits [13]. The closed-form solutions of these equations are valid for small separations between the spacecraft and neglect perturbation forces. On the contrary, averaging theory [59] can be used to first incorporate non-Keplerian perturbations (from conservative and non-conservative forces, including maneuvers) and then expand Eq. 50.4 into a Taylor expansion around the reference orbit elements [63]. Neglecting second order terms in the ROE which are multiplied by non-null partial derivatives leads to a linear dynamics system which is valid in the presence of perturbations and for nearly arbitrary separations between the spacecraft. The reduced accuracy of semi-analytical propagation or linear dynamics systems can be partially compensated through the estimation of empirical accelerations in the form a first-order Gauss-Markov process. The following paragraphs illustrate the formal equivalence between absolute and relative state updates and two examples of linear relative dynamics models for formation-flying and rendezvous in unperturbed near-circular and perturbed eccentric orbits respectively.

50.2.1.1 **Dual Inertial State Representation**

Depending on the mission context, the estimator may solve for a combination of pure absolute/inertial states, or some combination of absolute and relative states. The architecture originally developed for NASA's Apollo missions was a "dual-inertial" formulation[2]. While the absolute/relative formulation may appear to be mathematically equivalent, computational considerations may choose one or the other to be favored in various application contexts. A general observation is that the dual-inertial formulation may be favorable for computations involving the state and state error covariance, and for “absolute” measurements such as undifferenced pseudorange, while the absolute/relative formulation may be favorable for computations involving satellite-to-satellite relative measurements. Reference [2] provides a comprehensive mathematical description of the dual-inertial formulation in the context of relative range, Doppler, and bearing measurements that one may easily adapt, using the methods of Chapter 49, to an architecture that involves GNSS measurements.

Here, we consider only two spacecraft, but the results are easily generalized. Let $\boldsymbol{x}_i = [\boldsymbol{r}_i^T, \boldsymbol{v}_i^T]^T,\ i = 1, 2$ denote the true state of spacecraft i, with $\boldsymbol{r}_i, \boldsymbol{v}_i$ the position and velocity vectors expressed in non-rotating coordinates centered on the primary central gravitational body. Based on mission requirements and receiver's measurements noise, any appropriate fidelity of dynamics may be directly utilized, e.g.

$$\dot{\boldsymbol{x}}_i = \begin{bmatrix} \boldsymbol{v}_i \\ -\frac{\mu}{\|\boldsymbol{r}_i\|^3}\boldsymbol{r}_i + \sum_j \boldsymbol{f}_j \end{bmatrix} \tag{50.5}$$

where μ represents the gravitational parameter of the central body and the specific forces $\boldsymbol{f}_j$ may include thrust, higher-order gravity, drag, solar radiation pressure, gravity from non-central bodies such as the moon and the sun, etc.

Let $\boldsymbol{e}_i = \hat{\boldsymbol{x}}_i - \boldsymbol{x}_i$, where $\hat{\boldsymbol{x}}_i$ is an estimate for the state of spacecraft i. Then, the error in the state estimate $\hat{\boldsymbol{x}} = [\hat{\boldsymbol{x}}_1^T, \hat{\boldsymbol{x}}_2^T]^T$ is $\boldsymbol{e} = [\boldsymbol{e}_1^T, \boldsymbol{e}_2^T]^T$, and the error covariance is

$$\boldsymbol{P} = \mathrm{E}\Big[\boldsymbol{e}\boldsymbol{e}^T\Big] = \begin{bmatrix} \boldsymbol{P}_1 & \boldsymbol{P}_{12} \\ \boldsymbol{P}_{12}^T & \boldsymbol{P}_2 \end{bmatrix} \tag{50.6}$$

Any linear unbiased estimate of $\boldsymbol{x}$ will have the following measurement update equation

$$\hat{\boldsymbol{x}}^+ = \hat{\boldsymbol{x}}^- + \boldsymbol{K}(\boldsymbol{y} - \boldsymbol{h}(\hat{\boldsymbol{x}}^-)) \tag{50.7}$$

where $\hat{\boldsymbol{x}}^-$ is the value of $\hat{\boldsymbol{x}}$ immediately prior to incorporating the observation, $\boldsymbol{y}$, and $\boldsymbol{h}(\hat{\boldsymbol{x}}^-)$ is an unbiased prediction of the measurement's value. The optimal gain is

$$\boldsymbol{K} = \boldsymbol{P}\boldsymbol{H}^T(\boldsymbol{H}\boldsymbol{P}\boldsymbol{H}^T + \boldsymbol{R})^{-1} \tag{50.8}$$

where $\boldsymbol{R}$ is the measurement noise covariance and $\boldsymbol{H} = \partial \boldsymbol{h}(\boldsymbol{x})/\partial \boldsymbol{x}|_{\hat{\boldsymbol{x}}^-}$. Partition the update as follows:

$$\begin{bmatrix}\hat{\boldsymbol{x}}_1^+\\ \hat{\boldsymbol{x}}_2^+\end{bmatrix} = \begin{bmatrix}\hat{\boldsymbol{x}}_1^-\\ \hat{\boldsymbol{x}}_2^-\end{bmatrix} + \begin{bmatrix}\boldsymbol{K}_1\\ \boldsymbol{K}_2\end{bmatrix}(\boldsymbol{y} - \boldsymbol{h}(\hat{\boldsymbol{x}}^-)) \tag{50.9}$$

$$= \begin{bmatrix}\hat{\boldsymbol{x}}_1^-\\ \hat{\boldsymbol{x}}_2^-\end{bmatrix} + \begin{bmatrix}\boldsymbol{P}_1\boldsymbol{H}_1^T + \boldsymbol{P}_{12}\boldsymbol{H}_2^T\\ \boldsymbol{P}_{12}^T\boldsymbol{H}_1^T + \boldsymbol{P}_2\boldsymbol{H}_2^T\end{bmatrix}(\boldsymbol{H}\boldsymbol{P}\boldsymbol{H}^T + \boldsymbol{R})^{-1}(\boldsymbol{y} - \boldsymbol{h}(\hat{\boldsymbol{x}}^-)) \tag{50.10}$$

from which it is clear that the optimal update for the relative state $\hat{\boldsymbol{x}}_{\text{rel}} = \hat{\boldsymbol{x}}_2 - \hat{\boldsymbol{x}}_1$ is

$$\hat{\boldsymbol{x}}_{\text{rel}}^+ = \hat{\boldsymbol{x}}_{\text{rel}}^- + (\boldsymbol{P}_2\boldsymbol{H}_2^T - \boldsymbol{P}_1\boldsymbol{H}_1^T - \boldsymbol{P}_{12}\boldsymbol{H}_2^T + \boldsymbol{P}_{12}^T\boldsymbol{H}_1^T)(\boldsymbol{H}\boldsymbol{P}\boldsymbol{H}^T + \boldsymbol{R})^{-1}(\boldsymbol{y} - \boldsymbol{h}(\hat{\boldsymbol{x}}^-)) \tag{50.11}$$

with corresponding relative error covariance

$$\boldsymbol{P}_{\text{rel}} = \boldsymbol{P}_1 + \boldsymbol{P}_2 - \boldsymbol{P}_{12} - \boldsymbol{P}_{12}^T \tag{50.12}$$

Noting that it must be true that $\boldsymbol{h}(\boldsymbol{x}_{\text{rel}}) = \boldsymbol{h}(\boldsymbol{x})$ and hence that $\partial \boldsymbol{h}(\boldsymbol{x}_{\text{rel}})/\partial \boldsymbol{x}_{\text{rel}} = \partial \boldsymbol{h}(\boldsymbol{x}_2)/\partial \boldsymbol{x}_2 = -\partial \boldsymbol{h}(\boldsymbol{x}_1)/\partial \boldsymbol{x}_1$, let $\boldsymbol{H}_{\text{rel}} = \boldsymbol{H}_2 = -\boldsymbol{H}_1$. Then it is clear that

$$\boldsymbol{P}_{\text{rel}}\boldsymbol{H}_{\text{rel}}^T = \boldsymbol{P}_2\boldsymbol{H}_2^T - \boldsymbol{P}_1\boldsymbol{H}_1^T - \boldsymbol{P}_{12}\boldsymbol{H}_2^T + \boldsymbol{P}_{12}^T\boldsymbol{H}_1^T \tag{50.13}$$

and that

$$\boldsymbol{H}_{\text{rel}}\boldsymbol{P}_{\text{rel}}\boldsymbol{H}_{\text{rel}}^T = \boldsymbol{H}\boldsymbol{P}\boldsymbol{H}^T \tag{50.14}$$

and hence

$$\hat{\boldsymbol{x}}_{\text{rel}}^+ = \hat{\boldsymbol{x}}_{\text{rel}}^- + \boldsymbol{P}_{\text{rel}}\boldsymbol{H}_{\text{rel}}^T(\boldsymbol{H}_{\text{rel}}\boldsymbol{P}_{\text{rel}}\boldsymbol{H}_{\text{rel}}^T + \boldsymbol{R})^{-1}(\boldsymbol{y} - \boldsymbol{h}(\hat{\boldsymbol{x}}_{\text{rel}}^-)) \tag{50.15}$$

Therefore, the dual inertial state update is mathematically equivalent to a direct update of the relative state.

50.2.1.2 **Linearized Relative Dynamics using Spherical Coordinates**

Let the position of a spacecraft be given by a set of right-handed spherical coordinates

$$\boldsymbol{r} = \rho\begin{bmatrix}\cos\phi\sin\theta\\ \sin\phi\\ \cos\phi\cos\theta\end{bmatrix} \tag{50.16}$$

where ρ is the distance from the central body to the spacecraft, θ is measured along some specified great circle of the central body, and ϕ is measured along a great circle of the central body that is normal to the former great circle, and contains the position vector, as Figure 50.6 depicts. Define a state vector as follows: $\boldsymbol{x} = [\rho, \dot{\rho}, \theta, \dot{\theta}, \phi, \dot{\phi}]$. If the only force on the spacecraft is point-mass gravity from the central body, then the equations of motion are given by

$$\dot{\boldsymbol{x}} = \boldsymbol{f}(\boldsymbol{x}) = \begin{bmatrix}\dot{\rho}\\ -\mu/\rho^2 + \rho\dot{\phi}^2 + \rho\dot{\theta}^2\cos^2\phi\\ \dot{\theta}\\ -2\dot{\rho}\dot{\theta}/\rho + 2\dot{\phi}\dot{\theta}\tan\phi\\ \dot{\phi}\\ -2\dot{\rho}\dot{\phi}/\rho - \dot{\theta}^2\cos\phi\sin\phi\end{bmatrix} \tag{50.17}$$

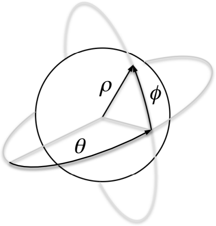

Figure 50.6 Spherical coordinates.

Now consider a circular reference orbit, with radius ρ_*, which is in the plane of the great circle containing the θ coordinate. Let $\omega_* = \sqrt{\mu/\rho_*^3}$. Then, the state of an object following the circular reference orbit at any time $t > t_o$ will be $\boldsymbol{x}_*(t) = [\rho_*, 0, \omega_*(t - t_o) - \theta_o, \omega_*, 0, 0]$. Without loss of generality, take $\theta_o = t_o = 0$. Letting $\delta\boldsymbol{x} = \boldsymbol{x} - \boldsymbol{x}_*$, linearization of (50.17) in the neighborhood of $\boldsymbol{x}_*$ yields

$$\delta\dot{\boldsymbol{x}}(t) = \left.\frac{\partial \boldsymbol{f}(\boldsymbol{x})}{\partial \boldsymbol{x}}\right|_{\boldsymbol{x}_*(t)} \delta\boldsymbol{x}(t) = \begin{bmatrix} 0 & 1 & 0 & 0 & 0 & 0 \\ 3\omega_*^2 & 0 & 0 & 2\omega_*\rho_* & 0 & 0 \\ 0 & 0 & 0 & 1 & 0 & 0 \\ 0 & -2\omega_*/\rho_* & 0 & 0 & 0 & 0 \\ 0 & 0 & 0 & 0 & 0 & 1 \\ 0 & 0 & 0 & 0 & -\omega_*^2 & 0 \end{bmatrix} \delta\boldsymbol{x}(t) \tag{50.18}$$

In this context, it is useful to redefine the state vector $\tilde{\boldsymbol{x}} = [\rho, \dot{\rho}, \rho_*\theta, \rho_*\dot{\theta}, \rho_*\phi, \rho_*\dot{\phi}]$ so that angles are replaced by arc lengths. Then, the linearized equations of motion become

$$\delta\dot{\tilde{\boldsymbol{x}}}(t) = \begin{bmatrix} 0 & 1 & 0 & 0 & 0 & 0 \\ 3\omega_*^2 & 0 & 0 & 2\omega_* & 0 & 0 \\ 0 & 0 & 0 & 1 & 0 & 0 \\ 0 & -2\omega_* & 0 & 0 & 0 & 0 \\ 0 & 0 & 0 & 0 & 0 & 1 \\ 0 & 0 & 0 & 0 & -\omega_*^2 & 0 \end{bmatrix} \delta\tilde{\boldsymbol{x}}(t) \tag{50.19}$$

If linearized relative dynamics are to be used for relative navigation in near-circular orbits, then interpreting the motion along the orbit track, and normal to the orbit track, as arc lengths, per the derivation above, is desirable since it will preserve the linearity of the approximation over a much wider range than if the along-track and cross-track coordinates are taken as rectilinear tangents to the reference orbit position. It is noted that this model is mathematically equivalent to the Hill-Clohessy-Wiltshire equations after replacing rectilinear with spherical coordinates.

50.2.1.3 **Linearized Relative Dynamics using Orbit Elements**

Let a, e, i, Ω, ω, and M denote the classical Keplerian orbit elements. For a formation consisting of two spacecraft including a chief, denoted by subscript c, and a deputy, denoted by subscript d, the simplest definition of ROE, $\delta\boldsymbol{\alpha}$, is given by

$$\delta\boldsymbol{\alpha} = \begin{pmatrix} \delta a \\ \delta M \\ \delta e \\ \delta\omega \\ \delta i \\ \delta\Omega \end{pmatrix} = \begin{pmatrix} (a_d - a_c)/a_c \\ M_d - M_c \\ e_d - e_c \\ \omega_d - \omega_c \\ i_d - i_c \\ \Omega_d - \Omega_c \end{pmatrix} \tag{50.20}$$

which is nearly identical to orbit element differences. The only difference in this definition is that the semi-major axis difference is normalized by the chief semi-major axis in order to keep all of the terms dimensionless.

Under the assumption of a Keplerian orbit, the time derivatives of the orbit elements are given as

$$\dot{a} = \dot{e} = \dot{i} = \dot{\omega} = \dot{\Omega} = 0 \qquad \dot{M} = n = \frac{\sqrt{\mu}}{a^{3/2}} \tag{50.21}$$

Because only M is time varying, the time derivative of the ROE state is given by

$$\delta\dot{\boldsymbol{\alpha}} = \begin{pmatrix} 0 \\ \dot{M}_d - \dot{M}_c \\ \mathbf{0}^{4\times 1} \end{pmatrix} = \sqrt{\mu} \begin{pmatrix} 0 \\ a_d^{-3/2} - a_c^{-3/2} \\ \mathbf{0}^{4\times 1} \end{pmatrix}. \tag{50.22}$$

The first-order Taylor expansion of Eq. 50.22 about zero separation is given as

$$\delta\dot{\boldsymbol{\alpha}}(t) = \begin{bmatrix} 0 & 0 & 0 & 0 & 0 & 0 \\ 0 & -1.5n & 0 & 0 & 0 & 0 \\ 0 & 0 & 0 & 0 & 0 & 0 \\ 0 & 0 & 0 & 0 & 0 & 0 \\ 0 & 0 & 0 & 0 & 0 & 0 \\ 0 & 0 & 0 & 0 & 0 & 0 \end{bmatrix} \delta\boldsymbol{\alpha}(t) = \mathbf{A}^{kep}(\boldsymbol{\alpha}_c)\delta\boldsymbol{\alpha}(t) \tag{50.23}$$

The range of applicability of this model can be assessed by determining which of the higher-order terms in the Taylor expansion given in Eq. 50.23 are non-zero. It is evident from Eq. 50.22 that Keplerian relative motion depends only on the semi-major axes of the spacecraft orbits. Accordingly, the only non-zero higher-order terms will be proportional to powers of δa. In contrast to Tschauner-Hempel and Hill-Clohessy-Wiltshire equations, this trivial relative motion model is valid for unperturbed orbits of arbitrary eccentricity with small δa and arbitrary separation in all other state components.

The Keplerian STM can be generalized to include the first-order secular effects of the second-order zonal geopotential harmonic, J_2. The J_2 perturbation causes secular drifts in M, ω, and Ω. These secular drift rates are given by Brouwer [64] as

$$\begin{pmatrix} \dot{M} \\ \dot{\omega} \\ \dot{\Omega} \end{pmatrix} = \frac{3}{4} \frac{J_2 R_E^2 \sqrt{\mu}}{a^{7/2}\eta^4} \begin{pmatrix} \eta(3\cos^2(i) - 1) \\ 5\cos^2(i) - 1 \\ -2\cos(i) \end{pmatrix} \tag{50.24}$$

The following substitutions are employed for brevity

$$\eta = \sqrt{1-e^2} \qquad \kappa = \frac{3}{4}\frac{J_2 R_E^2 \sqrt{\mu}}{a^{7/2}\eta^4} \qquad E = 1+\eta \qquad F = 4+3\eta \qquad G = \frac{1}{\eta^2} \tag{50.25}$$

$$P = 3\cos^2(i) - 1 \qquad Q = 5\cos^2(i) - 1 \qquad R = \cos(i) \qquad S = \sin(2i) \tag{50.26}$$

$$T = \sin^2(i) \qquad U = \sin(i) \qquad V = \tan(i/2) \qquad W = \cos^2(i/2) \tag{50.27}$$

The time derivatives of the ROE due to J_2 are computed by differentiating Eq. 50.20 with respect to time and substituting in the drift rates given in Eq. 50.24, yielding

$$\delta\dot{\boldsymbol{\alpha}} = \kappa_d \begin{pmatrix} 0 \\ \eta_d(3\cos^2(i_d) - 1) \\ 0 \\ 5\cos^2(i_d) - 1 \\ 0 \\ -2\cos(i_d) \end{pmatrix} - \kappa_c \begin{pmatrix} 0 \\ \eta_c(3\cos^2(i_c) - 1) \\ 0 \\ 5\cos^2(i_c) - 1 \\ 0 \\ -2\cos(i_c) \end{pmatrix} \tag{50.28}$$

The first-order Taylor expansion of Eq. 50.28 about zero separation is given as

$$\delta\dot{\boldsymbol{\alpha}}(t) = \kappa \begin{bmatrix} 0 & 0 & 0 & 0 & 0 & 0 \\ -\frac{7}{2}\eta P & 0 & 3e\eta GP & 0 & -3\eta S & 0 \\ 0 & 0 & 0 & 0 & 0 & 0 \\ -\frac{7}{2}Q & 0 & 4eGQ & 0 & -5S & 0 \\ 0 & 0 & 0 & 0 & 0 & 0 \\ 7R & 0 & -8eGR & 0 & 2U & 0 \end{bmatrix} \delta\boldsymbol{\alpha}(t) = \mathbf{A}^{J_2}(\boldsymbol{\alpha}_c)\delta\boldsymbol{\alpha}(t) \tag{50.29}$$

This plant matrix exhibits two useful properties. First, δa, δe, and δi are all constant. Second, the time derivatives of δM, $\delta\omega$, and $\delta\Omega$ depend only on these constant terms. Because of these properties, the J_2 state transition matrix for the ROE, $\boldsymbol{\Phi}^{J_2}(\boldsymbol{\alpha}_c(t_i), \tau)$, is simply expressed as

$$\boldsymbol{\Phi}^{J_2}(\boldsymbol{\alpha}_c(t_i), \tau) = \mathbf{I} + (\mathbf{A}^{kep}(\boldsymbol{\alpha}_c(t_i)) + \mathbf{A}^{J_2}(\boldsymbol{\alpha}_c(t_i)))\tau \tag{50.30}$$

The range of applicability of this model can be assessed by again considering higher-order terms of the Taylor expansion. It is evident from Eq. 50.28 that the time derivatives of the state elements do not depend on Ω, ω, or M. Accordingly, all partial derivatives of any order with respect to $\delta\Omega$, $\delta\omega$, and δM are zero. However, all second-order partial derivatives with respect to the remaining state elements are non-zero. It follows that this model is valid for small separations in δa, δe, and δi, but is valid for arbitrarily large separation in $\delta\Omega$, $\delta\omega$, and δM. As extensively discussed in Refs. [63, 65], this approach can be used to accurately capture effects of high-order gravity, atmospheric drag, solar radiation pressure and third body perturbations on the relative motion of large formations in closed-form. A simplified version of the state transition matrix given by Eq. 50.30 has been employed for relative GPS navigation in the TanDEM-X Autonomous Formation Flying (TAFF) system [45].

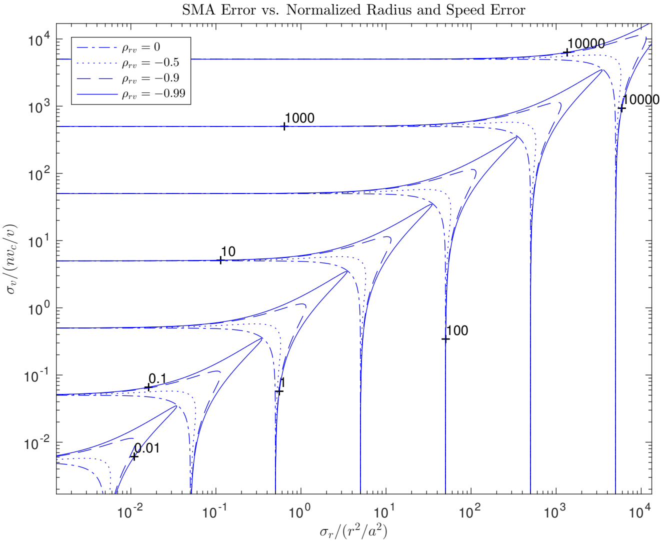

Figure 50.7 Contours of constant semi-major axis error (blue lines) show that the semi-major axis accuracy depends on radius error (σ_r, x-axis), speed error (σ_v, y-axis), their correlation (different line styles for correlation degree, ρ_{rv}), and their balance (along diagonal). All scales are in units of position.[66]

50.2.2
State Predictability

Orbit determination is distinguishable from other types of positioning and navigation not only by the use of dynamics suitable to orbiting bodies, but also by a fundamental need to produce states that predict accurately. This need arises because spacecraft operations require accurate predictions for acquisition by communications assets, for planning future activities such as maneuvers and observations, for predicting conjunctions with other space objects, etc. For closed, i.e. elliptical, orbits about most planetary bodies, the two-body potential dominates all other forces by several orders of magnitude. Thus, in most cases, the ability of an orbit estimate to predict accurately is dominated by semi-major axis (SMA) error, δa. This is because SMA error translates into period error through Kepler's third law, and an error in orbit period translates into a secularly increasing error in position along the orbit track. As Reference [66] shows, the along-track drift per orbit revolution, δs, for an elliptical orbit with eccentricity e is bounded by

$$\delta s = -3\pi\sqrt{\frac{1+e}{1-e}}\delta a \quad \text{from periapse to periapse} \tag{50.31}$$

$$\delta s = -3\pi\sqrt{\frac{1-e}{1+e}}\delta a \quad \text{from apoapse to apoapse} \tag{50.32}$$

$$\tag{50.33}$$

This phenomenon is especially significant for rendezvous and formation flying applications, where relative positions must be precisely controlled.

For a central body whose gravitational constant is μ, the SMA of a closed Keplerian orbit, a, may be found from the *vis viva* equation,

$$-\frac{\mu}{2a} = -\frac{\mu}{r} + \frac{v^2}{2} \tag{50.34}$$

from which one can see that achieving SMA accuracy requires good knowledge of both radius, r, and speed, v. What is less obvious from (50.34) is that radius and speed errors must also be both well-balanced and well-correlated to maximize SMA accuracy[67, 66, 68], as Figure 50.7 illustrates.

In this figure, radius error, σ_r, has been normalized by the squared ratio of radius to SMA, and speed error, σ_v, has been normalized by nv_c/v, where the orbital rate is $n = \sqrt{\mu/a^3}$, and the circular speed is $v_c = \sqrt{\mu/a}$, to make the relationships illustrated be independent of any particular closed orbit. Figure 50.7 shows contours of constant SMA error as blue lines with associated error σ_a in units of position. It is clear that σ_a is dominated by radius error below a diagonal region, and dominated by speed error above the diagonal. On the other hand, when radius and speed errors are balanced, along the diagonal, SMA accuracy can be substantially improved by increasing (negative) correlation, ρ_{rv}. Experience has shown that σ_a is one of the more useful figures of merit for evaluating orbit determination performance, particularly for relative navigation applications.

50.2.3
Estimation

A wide range of methods has been developed for relative orbit determination that may be divided into batch and sequential estimators. Batch least-squares estimation methods are primarily employed in post-processing, where data collected over a larger time span can be jointly processed to find the trajectory that best fits the entire set of measurements. Recursive estimation methods, in contrast, are favored in real-time applications, where they can provide new estimates of the instantaneous state vector at each measurement epoch. The batch least-squares orbit determination using GPS observations is typically characterized by a large number of estimation parameters. About 3,000 unknowns per spacecraft are needed to adjust epoch-wise clock offsets when processing a 24 h data arc at a 30 s sampling interval. About 500 parameters per spacecraft are needed for empirical accelerations, while the number of carrier-phase ambiguity parameters may range from a minimum of 500 to more than 1,000 (depending on the number of frequencies processed and the amount of phase discontinuities encountered in the data). To reduce the dimension of the resulting normal equations a pre-elimination of the clock parameters can be performed [1] by partitioning into clock offset and non-clock parameters (i.e., dynamical and ambiguity parameters). The sub-block of the normal matrix related to clock offset parameters is a pure diagonal matrix and can therefore be directly inverted and allows a formal elimination of these parameters from the normal equations. For precise relative navigation (or "baseline determination"), batch estimation strategies have so far been adopted by different researchers using the Bernese [36], EPOS-OC [69] and ZOOM [70] software packages. Here, trajectory parameters and float valued ambiguities for the ionosphere-free L1/L2 carrier phase combination of each individual spacecraft in the formation are first determined similar to a single satellite precise orbit determination. Thereafter double-difference ambiguities between GPS satellites and the formation flying spacecraft are resolved using a wide-lane/narrow-lane technique. Fixed ambiguities are then treated as additional constraints in a final orbit determination step that re-adjusts the (relative) trajectory and any unresolved ambiguity parameters.

Sequential estimation methods are a primary choice for on-board navigation systems requiring continuous information on the instantaneous formation geometry. Nevertheless, the concept has also been adopted for offline processing in Refs. [34, 35], since it reduces the number of ambiguity parameters that need to be simultaneously adjusted and fixed to the number of currently tracked channels. The most popular sequential estimation filter used in aerospace applications is the EKF. Its original and probably reputation-making application was the rendezvous navigation for the Apollo missions[71]. Although the EKF has been described in detail elsewhere in this book, including its application to orbit determination in Chapter 49, there are a number of considerations for its application to relative navigation, which are described in the following sections. Additionally, newer approaches to estimation, such as sigma-point/unscented Kalman filters, are gaining increasing acceptance in the aerospace community [72, 73], as further discussed in Chapter XX on nonlinear estimation techniques.

50.2.3.1 **Editing**

Let $r = y - h(x)$, where y is the observed measurement, $h(x)$ is the value of the measurement computed from the state x, $y = h(x) + v$, and v is the measurement noise, $\mathrm{E}[v] =$, $\mathrm{E}\left[vv^T\right] = R$. The quantity r is known as the *innovation* or sometimes the *residual*. The covariance of r is given by

$$W = HPH^T + R \tag{50.35}$$

where $P = \mathrm{E}\left[ee^T\right]$, $H = \partial h(x)/\partial x$, and e is the error in the estimate of x. The squared *Mahalanobis distance* associated with r,

$$m_r^2 = r^T W^{-1} r \tag{50.36}$$

has a χ^2 distribution with degrees of freedom equal to the number of measurements contained in the vector y. The statistic m_r^2, also known as the squared residual or innovations ratio, may be compared to a χ^2 statistic with a given probability in order to edit outlying measurements. For a purely linear estimation scheme, such editing is unnecessary, but for an *ad hoc* linearization such as the EKF, editing is essential to prevent large innovations that would violate Taylor series truncations used to develop the EKF approximation from being violated, even in the unlikely scenario in which sensors produced measurements with noise characteristics that perfectly followed their assumed (Gaussian) probability distributions.

50.2.3.2 **Underweighting**

An additional issue that arises due to the truncations involved in the EKF is that neglected second-order terms may become important, especially during initial filter convergence, even for highly accurate measurements. This can lead to Kalman filter “smugness”, in which the filter covariance matrix becomes exceedingly and artificially small. The technique of *meaurement underweighting* has evolved to deal with such situations. In its simplest form, underweighting involves use of a measurement noise covariance in the Kalman filter than is larger than would otherwise be suggested by the sensor noise specifications. Various practitioners have developed more sophisticated mechanisms, and Zanetti[74] provides a survey and comparison among several.

50.2.3.3 **Factorization**

From the time of the original Kalman filtering applications, developers observed that even with double-precision arithmetic, truncation and roundoff errors invariably lead to indefinite representations of covariance matrices in the Kalman filter algorithm. Bierman's UD factorization [75] of the EKF has emerged as the principal computational method to mitigate many such issues.

50.2.3.4 **Bias Modeling**

Most sensors possess errors that are characterized by noise and bias. Estimation, or otherwise consideration, of measurement biases is often required to achieve required estimation performance. Inappropriate bias models may lead to poor performance. For example, use of a random constant model, with no process noise, can lead to Kalman filter smugness. This can lead to inaccurate Kalman gain calculations, and in the context of an editing scheme, cause measurements to be rejected inappropriately, either of which may lead to filter divergence. Use of a random walk model with excessive process noise may lead to word length overflow if the bias is propagated for long enough intervals without stimulation by measurements with which it is associated. Therefore stable bias models, e.g.[76], are advisable, especially for poorly observed solve-for states, or for “consider” states, for which the filter maintains a covariance, but does not perform state updates[77]. A wide class of random processes can be approximated by first-order exponentially correlated process noise (or colored noise) [75]. A recursive mathematical description of such a process is

$$y(t) = \phi(t, t_0)y(t_0) + w(t) \tag{50.37}$$

with the state parameter y, state transition function ϕ, and process noise w. The model of the random process is given by

$$\phi = e^{-(t-t_0)/\tau} \tag{50.38}$$

τ being the correlation time constant of the process, and

$$w = w_\delta \sqrt{\frac{\sigma^2 \tau}{2}(1-\phi^2)} \tag{50.39}$$

w and w_δ are white, zero mean, Gaussian noise characterized by variance

$$E(w^2) = q = \sigma^2(1-\phi^2) \qquad\qquad E(w_\delta^2) = \delta(t-t_0) \tag{50.40}$$

where $\delta(t)$ is the Dirac delta function. Vector-valued colored-noise problems are comprised of concatenations of scalar processes. The degree of correlation of the random process ϕ is determined by the choice of σ and τ which can be tuned, or even estimated, to generate several time correlated random functions. In relative orbit determination, the colored noise is well suited to model the empirical accelerations in the radial, along-track and cross-track direction. These parameters are considered to compensate for any modeling deficiencies in the employed spacecraft dynamics. Furthermore the usage of process noise in an EKF is shown to improve overall accuracy and maintain non-negativity and symmetry of the computed covariance. Considering typical orbital periods of roughly 5000 s for LEO satellites and representative measurement intervals of 30 s, a correlation time constant of 900 s is found to be well suitable for sequential estimation of the empirical accelerations (cf. [33]). Equation 50.38 is used to compute the individual entries of the empirical accelerations in the state transition matrix. The described process noise model reduces to a white noise sequence in the case $\tau = 0$, which gives $y(t) = w(t)$. On the other extreme, for a finite value of σ^2 and $\tau = \infty$, the model reduces to $y(t) = y(t_0) + w(t)$, which describes a random walk process. The latter is usually adopted to model the user clock offset, with a resulting scalar mapping factor of $\phi_{c\delta t} = 1$ and a process noise that can be obtained from Eq. 50.39 with $\tau = \infty$ as

$$w_{c\delta t} = w_\delta \sigma_{c\delta t} \sqrt{t - t_0} \tag{50.41}$$

The variance of such a random walk process model is given by

$$q_{c\delta t} = \sigma^2_{c\delta t}(t - t_0)/\tau_{c\delta t} \tag{50.42}$$

Depending on the adopted model, colored noise for empirical accelerations and random walk for GPS receiver clock offsets, Eqs. 50.40 and 50.42 are used to update the EKF covariance. An important aspect to consider in relative orbit determination is the degree of cross-correlation of estimation parameters related to individual spacecraft. While clock offsets of different receivers are entirely uncorrelated, empirical accelerations are potentially highly correlated due to the common forces exterted on the co-orbiting spacecraft. In particular, the uncertainty associated with the (absolute) dynamics model of a single satellite motion is generally much higher than the uncertainty associated with the (relative) dynamics model for a spacecraft formation. Especially for dual-inertial symmetric filters which process both coarse pseudorange and precise single-difference carrier-phase measurements, the a-priori covariance of the absolute empirical accelerations should be set so to properly constraint the covariance of the relative empirical accelerations at the same time. Specifically, instead of defining the covariance of the empirical accelerations $\boldsymbol{a}$ of spacecraft 1 and 2 as

$$\boldsymbol{P}(\boldsymbol{a}_1, \boldsymbol{a}_2) = \begin{bmatrix} \boldsymbol{\sigma}^2(\boldsymbol{a}_1) & \boldsymbol{0} \\ \boldsymbol{0} & \boldsymbol{\sigma}^2(\boldsymbol{a}_2) \end{bmatrix} \tag{50.43}$$

absolute and relative dynamics can be constrained independently through

$$\boldsymbol{P}(\boldsymbol{a}_1, \boldsymbol{a}_2) = \begin{bmatrix} \boldsymbol{1} & \boldsymbol{0} \\ \boldsymbol{1} & \boldsymbol{1} \end{bmatrix} \begin{bmatrix} \boldsymbol{\sigma}^2(\boldsymbol{a}_1) & \boldsymbol{0} \\ \boldsymbol{0} & \boldsymbol{\sigma}^2(\boldsymbol{\Delta a}) \end{bmatrix} \begin{bmatrix} \boldsymbol{1} & \boldsymbol{1} \\ \boldsymbol{0} & \boldsymbol{1} \end{bmatrix} = \begin{bmatrix} \boldsymbol{\sigma}^2(\boldsymbol{a}_1) & \boldsymbol{\sigma}^2(\boldsymbol{a}_1) \\ \boldsymbol{\sigma}^2(\boldsymbol{a}_1) & \boldsymbol{\sigma}^2(\boldsymbol{a}_1) + \boldsymbol{\sigma}^2(\boldsymbol{\Delta a}) \end{bmatrix} \tag{50.44}$$

where $\boldsymbol{\Delta a} = \boldsymbol{a}_2 - \boldsymbol{a}_1$ represents the differential empirical acceleration.

50.3
Mission results

Example flight results from the Space Shuttle, PRISMA, TanDEM-X, and MMS missions are presented in this section. Far from being complete, the intent is to demonstrate the versatility and broad range of applicability of GNSS relative navigation for formation-flying and rendezvous missions. Missions' context, goals, and descriptions are given in Section 50.1.1.

50.3.1
Space Shuttle

The overall history and experience of the Space Shuttle's GPS navigation is provided by [3, 4]. First results from the real-time relative GPS flight experiment on the Space Shuttle mission STS-69 in 1995 are presented in [6]. This experiment used GPS data from an Osborne/JPL TurboRogue receiver (4 channels) carried on the target Wake Shield Facility (WSF) free-flyer and a Rockwell Collins 3M receiver (8 channels) carried on the chaser Orbiter. A single GPS antenna was mounted on the WSF free-flyer, whereas two GPS antennas were mounted on the Orbiter with opposite field of view. The real-time GPS (RGPS) KF processes pseudorange measurements from both vehicles and estimate their absolute position and velocity in the earth-centered earth-fixed (ECEF) reference frame, together with clock offsets/drifts, empirical accelerations for the chaser, and a total of 12 range biases for each channel of the GPS receivers to accomodate Selective Availability (SA) and other unmodelled radio-frequency delays. The dynamics model includes geopotential coefficients up to order/degree 30 (typically set to 4), and accelerometer measurements during powered flight. Since continuous WSF GPS data never became available during WSF rendezvous, to complete the performance analysis, the RGPS was ran in real-time mode using recorded data.

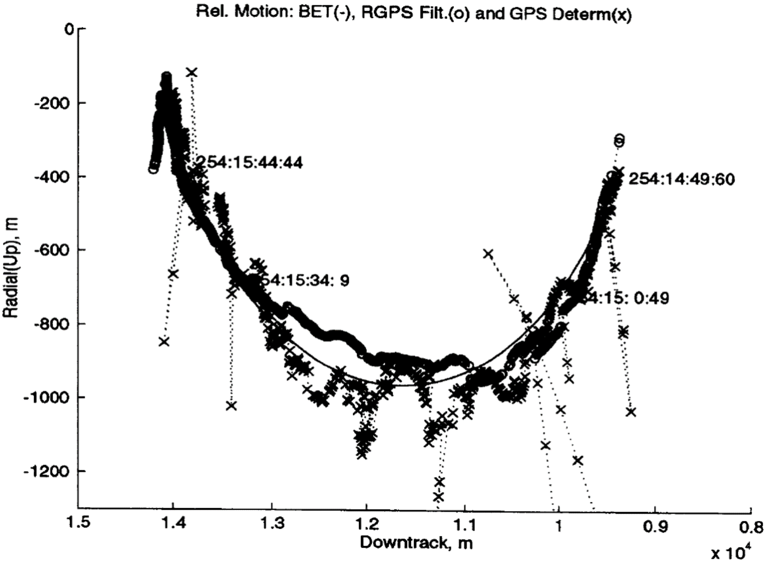

Figure 50.8 Target centered relative motion plot during STS-69 in LVLH frame (radial vs downtrack) during 1 hour of rendezvous as given by different sources of relative navigation: 1) Best Estimate Trajectory (BET) based on double-differencing and GPS ground-stations (-), 2) Playback of on-board RGPS (o), 3) Navigation solutions from receiver (x) [6].

Figure 50.8 shows the relative trajectory in LVLH coordinates over a time interval of about 1 hour as obtained by three different sources: 1) the Best Estimate Trajectory (BET) determined by the University of Texas Center for Space Research using double-differencing GPS data from both vehicles along with data from GPS ground stations, 2) the playback of RGPS, and 3) the GPS receiver deterministic solutions. As expected, the RGPS compares more favorably to the BET than does the receiver deterministic solution. Overall the RGPS filter performance achieved steady-state errors in relative semi-major axis estimation below 100 m with good consistency of formal covariance. This was quite satisfactory given the different employed receivers, unexpected clock offset problems with the TurboRogue receiver, the reduced number of available commonly visible satellites (< 4), in combination with the adverse effects of SA. Despite the many hardware and software glitches encountered during the mission, valuable lessons were learned in relative GPS navigation which paved the way for future Space Shuttle experiments and rendezvous missions to the ISS.

50.3.2
PRISMA

A comprehensive overview of the PRISMA's guidance, navigation, and control system and its hardware and software experiments is given in [20]. Key flight results from the real-time relative GPS navigation system are presented in [19, 22, 24, 25]. PRISMA employs identical DLR's single-frequency 12-channel Phoenix GPS receivers on both spacecraft of the formation in a cold-redundant configuration. Each spacecraft embarks two patch antennas on opposite sides for near-omnidirectional visibility. A RF switch allows the selection of the GPS antenna in use, either from ground or autonomously on-board as a function of the attitude. The real-time relative navigation system is a dual-inertial EKF which processes GRAPHIC data types and single-difference carrier-phase measurements to estimate spacecraft position/velocity, receivers' clock offsets, empirical accelerations, carrier-phase float biases on each channel, force model parameters, and maneuver's delta-v executed by the active satellite (Mango). The dynamics model includes geopotential coefficients up to order/degree 20, atmospheric drag, solar radiation pressure and third body forces from the Sun/Moon.

Figure 50.9 provides the typical navigation accuracy obtained on the PRISMA mission in flight. As compared with the on-ground precise orbit determination product, the relative position and velocity errors are about 5.12 cm and 0.21 mm/s (3D, rms) respectively and thus well below the formal requirement of 0.2 m and 1 mm/s defined at the beginning of the mission. It is noted that the tuning of the navigation filter plays a key role in the achievable accuracy, and especially the weights of measurement noise and a-priori standard deviation of the empirical accelerations have to be carefully considered. As an example, the filter settings applied during the scenarios in Fig. 50.9 introduce large empirical accelerations in radial direction as compared to the other components. The resulting loose constraint on the relative dynamics causes larger errors in radial direction, but is shown to be beneficial for the absolute orbit determination accuracy which amounts to 2 m and 7.5 mm/s (3D, rms) for position and velocity respectively.

50.3.3
TanDEM-X

The design of the TanDEM-X Autonomous Formation Flying system (TAFF) is addressed in [43]. Flight results from the real-time relative GPS navigation system are presented in [45, 78]. TAFF employs identical Astrium EADS' single-frequency 10-channels Mosaic GNSS receivers on both spacecraft. The real-time relative navigation system processes ECEF navigation solutions in an EKF which estimates quasi-nonsingular relative orbit elements [18]. The dynamics model relies on a state

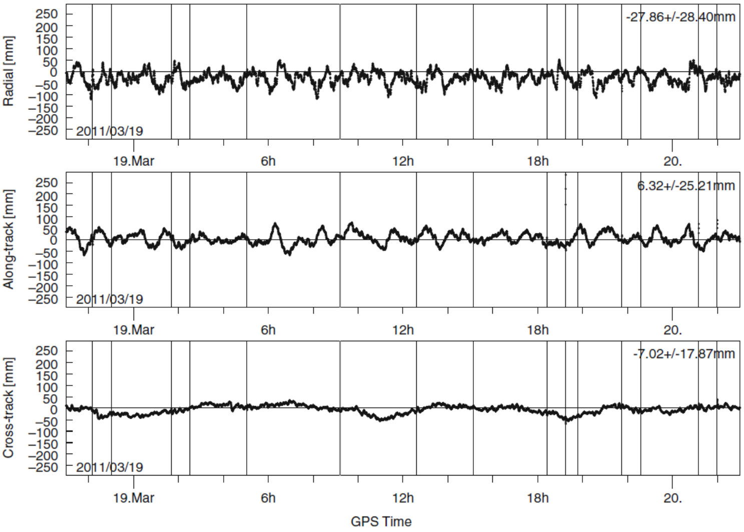

Figure 50.9 Difference of real-time on-board navigation solution versus post-facto on-ground precise orbit product for PRISMA on March 19, 2011 in RTN frame. Orbit control maneuvers for autonomous closed-loop formation control are indicated by vertical lines [20].

transition matrix which includes secular earth's oblateness J_2 effects.

Figure 50.10 depicts the daily errors (rms values) of the on-board estimated relative orbit elements compared with precise orbit products over three months in 2011. Special attention needs to be paid to the on-board estimates of the relative semi-major axis Δa and of the dimensioned relative eccentricity vector $a\Delta\boldsymbol{e}$. These two relative orbit elements are of special relevance in the relative orbit control scheme. The first quantity drives the drift between the satellites. As a consequence its accurate estimation is necessary to ensure a precise control of the along-track separation. The second quantity is used to compute the location of the maneuvers. Considering the fact that TAFF is allowed to execute maneuvers only on a restricted part of the orbit, the accurate estimation of $a\Delta\boldsymbol{e}$ is of great importance to ensure that no maneuver will be executed during the acquisition of SAR images. Overall the estimate of Δa is accurate to 20 cm and the other relative orbit elements are accurate at the sub-meter level, except the along-track component $a\Delta u$ whose error can reach a few meters.

50.3.4
MMS

GPS Navigation for the MMS mission is covered in [31, 32]. Recent flight results and simulations at cis-lunar altitudes are presented in [79, 80]. MMS embarks two GSFC's Navigator GPS receivers on each of the four satellites for navigation in high elliptical orbit above the GPS constellation. Each receiver is connected to one Ultra-Stable Oscillator (USO), made by Frequency Electronics, Inc., and four GPS antennas, developed in house at GSFC, with associated front-end electronics assembly,

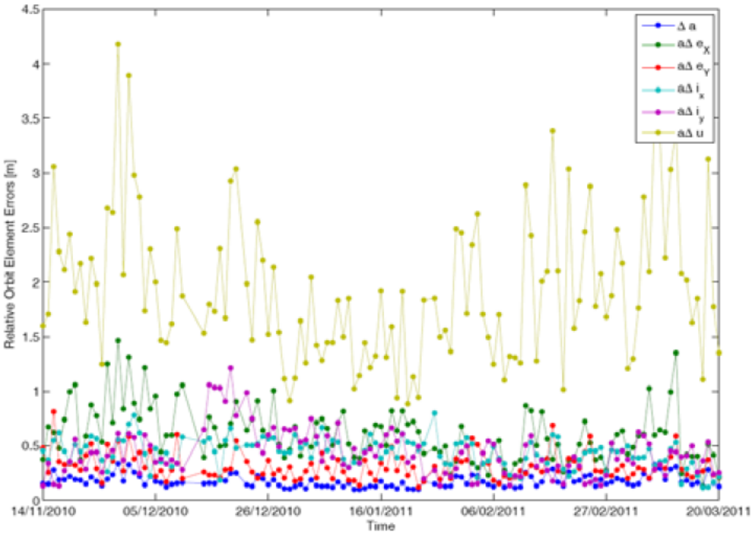

Figure 50.10 Long-term analysis of real-time relative orbit elements navigation errors obtained by TAFF in orbit [78].

developed by Delta-Microwave, Inc. To cope with the satellite spinning at 3 RPM, the antennae are equally spaced around the perimeter to allow for hand-off every five seconds. The on-board GEONS' EKF estimates the spacecraft position/velocity, clock bias/drift/acceleration. GEONS processes up to 12 GPS L1 C/A pseudorange measurements on a 30 second estimation cycle. The dynamics model includes the geopotential to order/degree 13, solar and lunar point masses, solar radiation pressure, atmospheric drag, and incorporates 10-second averaged measurements from the accelerometer during maneuvers.

Figure 50.11 (left) shows the number of signals tracked along with the corresponding radial distance during three orbits in 2017. Only one spacecraft is shown in the plot, but the performance for the other three satellites is almost identical. On average about three signals are tracked near apogee, and point solutions at 25 RE are obtained regularly. This significantly exceeds the zero, one, or two mainlobe-only signals that were predicted during pre-flight analysis. The excellent visibility above the GPS constellation is due to Navigator's ability to acquire and track weak GPS transmitter side-lobe signals with signal-to-noise ratios below 30 dB-Hz. Figure 50.11 (right) shows the GEONS' position and velocity RSS (1σ) root-covariance diagonal "formal errors". The maximum RSS formal errors reach about 50 m just prior to returning to perigee and the maximum RSS velocity formal errors spike to a bit above 2 mm/s near perigee entry, where the filter makes a large correction, otherwise remaining near 1 mm/s. These errors correspond to a 1σ formal error of about 15 m in semi-major axis, far less than the mission requirement of 100 m. Clearly, MMS shows that GPS navigation at high-altitude can provide excellent performance, simplify operations, and provide cost benefits to missions. Analyses conducted in the frame of the MMS mission indicate that robust autonomous GPS navigation performance is achievable at Lunar distances.

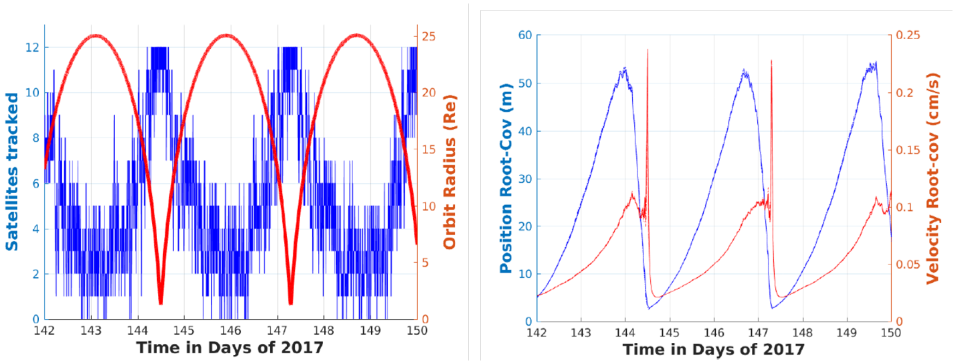

Figure 50.11 GEONS' 1σ formal error (root-covariance) over three orbits of MMS during Phase 2B (right). Number of signals tracked and radial distance (left) [79].

50.4
Conclusions

GNSS-based relative navigation is an enabling technology for distributed space systems, including spacecraft rendezvous (for in-orbit assembly and servicing), formation-flying (for earth/planetary science and astronomy/astrophysics), and swarms (for environment sampling) architectures. The intensive research and numerous flight demonstrations conducted in the past decades have clearly demonstrated the suitability of GNSS relative navigation for operations at diverse orbit regimes (low-circular and high-elliptic earth orbits, cis-lunar), spacecraft separations (zero to hundreds of kilometers), accuracy requirements (mm- to m-level navigation errors), and for different applications (closed-loop on-orbit control, precise baseline estimation for science data processing on-ground). This chapter has provided an overview of the key historical landmarks of GNSS-based relative navigation, from the pioneering activities of the Gemini program in the 1960s, through the most recent demonstrations of autonomous small satellite formation-flying, all the way to groundbreaking science missions for global time-varying earth's gravity/shape recovery and magnetospheric study at multiple scales. Potential and future applications have been discussed, including precision formation-flying in earth's orbit to study the corona of the Sun and nanosatellite swarms for gigantic synthetic apertures and satellite aggregation applications.

Since the availability of an adequate relative navigation system is a prerequisite to the success of these missions, this chapter has presented the state-of-the-art of key aspects that need to be carefully considered during the design and development: state representation, dynamics models, and estimation approach. Several options are available that need to be properly traded for the mission of interest. It has been shown how a wide range of different estimation parameters can be considered, including the spacecraft motion described by position/velocity or orbit elements, the dynamics model parameters such as atmospheric/solar radiation pressure coefficients, maneuver delta-v, and empirical accelerations, and measurement model parameters such as receivers' clock-offsets, carrier-phase ambiguities, and ionospheric path delays. Most of these parameters can either be handled as absolute quantities (i.e., referring to a single spacecraft) or relative quantities (i.e., describing the difference of a parameter for one satellite relative to a reference spacecraft in the formation) and both representations can be rigorously transformed into each other. The dynamics model can be based on the numerical integration of the equations of absolute/relative motion for utmost accuracy or approximations thereof such as from linearization and averaging theory for computational simplicity and efficiency. Examples of simple yet powerful linearized relative dynamics models have been illustrated, including state representations in spherical coordinates and relative orbit elements. Key aspects of batch and sequential estimation for relative navigation have been addressed, including data editing, underweighting, factorization, and bias modeling using colored process noise. Finally, flight results from a number of satellite rendezvous and formation-flying missions have been presented. The very first in-flight demonstrations of GPS relative navigation with meter-level accuracy have been performed in the 1990s as part of various national rendezvous programs. These paved the way for more advanced demonstrations two decades later exploiting the full potential of differential carrier-phase techniques. Although much better performances could later be achieved in hardware-in-the-loop simulations using GPS signal simulators, it is only since the GRACE mission that the feasibility of reconstructing the relative position between co-orbiting spacecraft with mm-level accuracy has been proven. Nowadays, the 3D baseline between the TanDEM-X satellites, the first synthetic aperture radar interferometer in orbit, can be routinely determined with a consistency of 1–2 mm on-ground. Moreover the high technology readiness level reached by real-time relative GPS is clearly demonstrated by formation-flying satellites such as PRISMA and Can-X whose relative motion has been autonomously controlled on a regular basis using a cm-accurate GPS-based relative navigation system as primary sensor. Finally, the highest-altitude operational usage of GPS to date has been accomplished in the frame of the MMS mission. Formal semi-major axis estimation errors of a few tens of meters obtained at 25 Earth radii while tracking 4-6 GPS satellites are a testament of the potential of reduced-dynamics orbit determination in combination with weak signal tracking of the transmitter sidelobes.

References

1 Montenbruck, O. and D'Amico, S. (2013) *Distributed Space Missions for Earth System Monitoring*, Springer, Space Technology Library, vol. 31, chap. GPS Based Relative Navigation, pp. 185–223.

2 Muller, E.S. and Kachmar, P.M. (1971–72) A new approach to on-board orbit navigation. *Navigation: Journal of the Institute of Navigation*, **18** (4), 369–385.

3 Goodman, J.L. (2006) History of space shuttle rendezvous and proximity operations. *Journal of Spacecraft and Rockets*, **43** (5), 944–959.

4 Goodman, J.L. (2001) Space shuttle navigation in the gps era, in *Proceedings of the 2001 National Technical Meeting of The Institute of Navigation*, Long Beach, CA, pp. 709–724.

5 Hinkel, H., Park, Y., and Fehse, W. (1995) Real-time gps relative navigation flight experiment, in *Proceedings of the 1995 National Technical Meeting of The Institute of Navigation*, Anaheim, CA, pp. 593–601.

6 Park, Y.W., Brazzel, J.P., Carpenter, J.R., Hinkel, H.D., and Newman, J.H. (1996) Flight test results from real-time relative gps experiment on sts-69, in *SPACEFLIGHT MECHANICS 1996*, *Advances in the Astronautical Sciences*, vol. 93, Univelt, San Diego, CA, *Advances in the Astronautical Sciences*, vol. 93, pp. 1277–1296.

7 Schutz, B., Abusali, P., Schroeder, C., Tapley, B., Exner, M., McCloskey, R., Carpenter, R., Cooke, M., McDonald, S., Combs, N., Duncan, C., Dunn, C., and Meehan, T. (1995) Gps tracking experiment of a free-flyer deployed from space shuttle, in *Proceedings of the 8th International Technical Meeting of the Satellite Division (ION–GPS)*, The Institute of Navigation, Alexandria, VA, pp. 229–235.

8 Moreau, G. and Marcille, H. (1997) Rgps postflight analysis of arp-k flight demonstration, in *Proceedings of the 12th international symposium on spaceflight dynamics*, Darmstadt, Germany, ESA SP–403, pp. 97–102.

9 Schiesser, E., Brazzel, J.P., Carpenter, J.R., and Hinkel, H.D. (1998) Results of sts-80 relative gps navigation flight experiment, in *SPACEFLIGHT MECHANICS 1998*, *Advances in the Astronautical Sciences*, vol. 99, Univelt, San Diego, CA, *Advances in the Astronautical Sciences*, vol. 99, pp. 1317–1334.

10 Moreau, G. and Marcille, H. (1998) On-board precise relative orbit determination, in *Proceedings of the 2nd European symposium on global navigation satellite systems*, Toulouse, France.

11 Kawano, I., Mokuno, M., Kasai, T., and Suzuki, T. (2001) First autonomous rendezvous using relative gps navigation by ets-vii. *Navigation: Journal of the Institute of Navigation*, **48** (1), 49–56.

12 Kawano, I., Mokuno, M., Miyano, T., and Suzuki, T. (2000) Analysis and evaluation of gps relative navigation using carrier phase for rvd experiment satellite of ets-vii, in *Proceedings of the 2000 Institute of Navigation, ION-GPS-2000*, Salt Lake City, Utah.

13 Clohessy, W.H. and Wiltshire, R.S. (1960) Terminal guidance for satellite rendezvous. *Journal of the Aerospace Sciences*, **27** (5), 653–658, 674.

14 Cavrois, B., Personne, G., Stramdmoe, S., Reynuad, S., and Narmada Zink, M. (2008) Two different implemented relative position/velocity estimations using gps sensors on-board atv, in *Proceedings of the 7th ESA Conference on Guidance, Navigation and Control Systems, ESA-GNC-2008*, Tralee, Ireland.

15 Zanetti, R., Holt, G., Gay, R., D'Souza, C., Sud, J., Mamich, H., and Gillis, R. (2017) Design and flight performance of the orion pre-launch navigation system. *Journal of Guidance, Control and Dynamics*, **40** (9), 2289–2300.

16 D'Amico, S., Pavone, M., Saraf, S., Alhussien, A., Al-Saud, T., Buchman, S., Byer, R., and Farhat, C. (2015) Miniaturized autonomous distributed space system for future science and exploration, in *Proceedings of the 8th International Workshop on Satellite Constellations and Formation Flying, IWSCFF 2015*, Delft University of Technology, The Netherlands.

17 Folta, D. and Hawkins, A. (2002) Results of nasa's first autonomous formation flying experiment: Earth observing-1 (eo-1), in *Proceedings of the 2002 AIAA/AAS Astrodynamics Specialist Conference*, AIAA, Monterey, CA.

18 D'Amico, S. (2010) *Autonomous formation flying in low earth orbit*, Ridderprint BV, Technical University of Delft.

19 D'Amico, S., Ardaens, J.S., and Larsson, R. (2012) Spaceborne autonomous formation-flying experiment on the prisma mission. *Journal of Guidance, Control and Dynamics*, **35** (3), 834–850.

20 D'Amico, S., Bodin, P., Delpech, M., and Noteborn, R. (2013) *Distributed Space Missions for Earth System Monitoring*, Springer, Space Technology Library, vol. 31, chap. PRISMA, pp. 599–637.

21 D'Amico, S., Ardaens, J.S., DeFlorio, S., Montenbruck, O., Persson, S., and Noteborn, R. (2010) Gps-based spaceborne autonomous formation flying experiment (safe) on prisma: Initial commissioning, in *Proceedings of the AIAA/AAS Astrodynamics Specialist Conference*, Toronto, Canada.

22 D'Amico, S., Ardaens, J.S., and Montenbruck, O. (2011) Final commissioning of the prisma gps navigation system, in *Proceedings of the 22nd International Symposium on Spaceflight Dynamics*, Sao Jose dos Campos, Brazil.

23 D'Amico, S., Ardaens, J.S., and Larsson, R. (2011) In-flight demonstration of formation control based on relative orbital elements, in *Proceedings of the 4th International Conference on Spacecraft Formation Flying Missions and Technologies*, St-Hubert, Quebec.

24 Larsson, R., D'Amico, S., Noteborn, R., and Bodin, P. (2011) Gps navigation based proximity operations by the prisma satellites – flight results, in *Proceedings of the 4th International Conference on Spacecraft Formation Flying Missions and Technologies*, St-Hubert, Quebec.

25 Ardaens, J.S., Montenbruck, O., and D'Amico, S. (2010) Functional and performance validation of the prisma precise orbit determination facility, in *Proceedings of the ION International Technical Meeting*, San Diego, CA.

26 Bonin, G., Roth, N., Armitage, S., Newman, J., Risi, B., and Zee, R.E. (2015) Canx-4 and canx-5 precision formation flight: Mission accomplished!, in *Proceedings of the 29th Annual AIAA/USU Conference on Small Satellites*, Logan, UT.

27 Tapley, B., Bettadpur, S., Watkins, M., and Reigber, C. (2004) The gravity recovery and climate experiment: Mission overview and early results. *Geophys Res Lett*, **31** (9), L09 607.

28 Bertiger, W., Bar-Sever, Y., Desai, S., Dunn, C., Haines, B., Kruizinga, G., Kuang, D., Nandi, S., Romans, L., Watkins, M., Wu, S., and Bettadpur, S. (2002) Grace: millimeters and microns in orbit, in *Proceedings of ION-GPS-2002*, Portland, Oregon, p. 2022–2029.

29 Krieger, G., Moreira, A., Fiedler, H., Hajnsek, I., Werner, M., Younis, M., and Zink, M. (2007) Tandemx: a satellite formation for high resolution sar interferometry. *IEEE Trans Geosci Rem Sens*, **45** (11), 3317–3341.

30 Fiedler, H., Krieger, G., Werner, M., Reiniger, K., Diedrich, E., Eineder, M., D'Amico, S., and Riegger, S. (2006) The tandem-x mission design and data acquisition plan, in *Proceedings of the 6th European Conference on Synthectic Aperture Radar*, Dresden, Germany.

31 Winternitz, L.B., Bamford, W.A., Price, S.R., Carpenter, J.R., Long, A.C., and Farahmand, M. (2016) Global positioning system navigation above 76,000 km for nasa's magnetospheric multiscale mission, in *(to appear in) Guidance and Control 2016*, Univelt.

32 Farahmand, M., Long, A., and Carpenter, R. (2015) Magnetospheric multiscale mission navigation performance using the goddard enhanced onboard navigation system, in *Proceedings of the 25th International Symposium on Space Flight Dynamics*, www.issfd.org.

33 Kroes, R. (2006) *Precise Relative Positioning of Formation-Flying Spacecraft using GPS*, Technical University of Delft.

34 Kroes, R., Montenbruck, O., Bertiger, W., and Visser, P. (2005) Precise grace baseline determination using gps. *GPS Solutions*, **9**, 21–31.

35 Wu, S.C. and Bar-Sever, Y. (2006) Real-time sub-cm differential orbit determination of two low-earth orbiters with gps bias fixing, in *Proceedings of the ION GNSS 2006*, Fort Worth, TX.

36 Jaggi, A., Hugentobler, U., Bock, H., and Beutler, G. (2007) Precise orbit determination for grace using undifferenced or doubly differenced gps data. *Adv Space Res*, **39**, 1612–1619.

37 Kohlhase, A., Kroes, R., and D'Amico, S. (2006) Interferometric baseline performance estimations for multistatic sar configurations derived from grace gps observations. *Journal of Geodesy*, **80** (1), 28–39.

38 Montenbruck, O., Wermuth, M., and Kahle, R. (2010) Gps-based relative navigation for the tandem-x mission – first flight results, in *Proceedings of the ION GNSS 2010*, Portland, Oregon.

39 Wermuth, M., Montenbruck, O., and Wendleder, A. (2011) Relative navigation for the tandem-x mission and evaluation with dem calibration results, in *Proceedings of the 22nd International Symposium on Spaceflight Dynamics*, Sao Jose dos Campos, Brazil.

40 D'Amico, S., Arbinger, C., Kirschner, M., and Campagnola, S. (2004) Generation of an optimum target trajectory for the terrasar-x repeat observation satellite, in *Proceedings of the 18th International Symposium on Space Flight Dynamics, ISSFD 2004*, Munich, Germany.

41 Kahle, R. and D'Amico, S. (2014) The terrasar-x precise orbit control – concept and flight results, in *Proceedings of the 24th International Symposium on Space Flight Dynamics, ISSFD 2014*, Laurel, US.

42 D'Amico, S. and Montenbruck, O. (2006) Proximity operations of formation flying spacecraft using an eccentricity/inclination vector separation. *Journal of Guidance, Control and Dynamics*, **29** (3), 554–563.

43 Ardaens, J.S. and D'Amico, S. (2009) Spaceborne autonomous relative control system for dual satellite formations. *Journal of Guidance, Control and Dynamics*, **32** (6), 1859–1870.

44 Kahle, R., Schlepp, B., and Kirschner, M. (2011) Terrasar-x/tandem-x formation control — first results from commissioning and routine operations, in *Proceedings of the 22nd International Symposium on Space Flight Dynamics, ISSFD 2011*, Sao Jose dos Campos, Brazil.

45 Ardeans, J., D'Amico, S., and Fischer, D. (2011) Early flight results from the tandem-x autonomous formation flying system, in *Proceedings of the 4th International Conference on Spacecraft Formation Flying Missions and Technologies*, St-Hubert, Canada.

46 Kayali, S., Morton, P., and Gross, M. (2017) International challenges of grace follow-on, in *Proceedings of the IEEE Aerospace Conference, 2017*, Big Sky, MT.

47 Moreira, A. and et al (2015) Tandem-l: A highly innovative bistatic sar mission for global observation of dynamic processes on the earth's surface. *Proceedings of the IEEE Geoscience and Remote Sensing Magazine*, **3** (2), 8–23.

48 Garcia, P., Praile, C., and Lozano, J.M. (2017) Operational flight dynamics system for proba-3 formation flying mission, in *Proceedings of the 9th International Workshop on Satellite Constellations and Formation Flying*, University of Colorado Boulder, CO.

49 Mesreau-Garreau, A. and et al (2011) Proba-3 high precision formation-flying mission, in *Proceedings of 4th International Conference on Spacecraft Formation Flying Missions and Technologies*, St-Hubert, Quebec.

50 Ardaens, J.S., D'Amico, S., and Cropp, A. (2013) Gps-based relative navigation for the proba-3 formation flying mission. *Acta Astronautica*, **91**, 341–355.

51 Roscoe, C., Westphal, J.J., and Bowen, J.A. (2017) Overview and gnc design of the cubesat proximity operations demonstration (cpod) mission, in *Proceedings of the 9th International Workshop on Satellite Constellations and Formation Flying*, University of Colorado Boulder, CO.

52 Giralo, V., Eddy, D., and D'Amico, S. (2017) Development and verification of the stanford gnss navigation testbed for spacecraft formation-flying. *Technical Note TN2017-001*.

53 Busse, F. and How, J. (2002) Demonstration of adaptive extended kalman filter for low earth orbit formation estimation using cdgps, in *Proceedings of ION-GPS-2002*, Portland, OR.

54 Roth, N., Urbanek, J., Johnston-Lemke, B., Bradbury, L., Armitage, S., Leonard, M., Ligori, M., Grant, C., Damaren, C., and Zee, R. (2011) System-level overview of canx-4 and canx-5 formation flying satellites, in *Proceedings of 4th International Conference on Spacecraft Formation Flying Missions and Technologies*, St-Hubert, Quebec.

55 Ebinuma, T., Bishop, R., and Lightsey, G. (2001) Spacecraft rendezvous using gps relative navigation, in *AAS 01–152, Proceedings of 11th annual AAS/AIAA Space Flight Mechanics Meeting*, Santa Barbara, CA.

56 D'Amico, S., Gill, E., Garcia-Fernandez, M., and Montenbruck, O. (2006) Gps-based real-time navigation for the prisma formation flying mission, in *Proceedings of 3rd ESA Workshop on Satellite Navigation User Equipment Technologies, NAVITEC'2006*, Noordwijk, The Netherlands.

57 Hill, G.W. (1878) Researches in the lunar theory. *American Journal of Mathematics*, **1** (1), 5–26, 129–147, 245–260.

58 Sullivan, J., Grimberg, S., and D'Amico, S. (2017) Comprehensive survey and assessment of spacecraft relative motion dynamics models. *Journal of*

Guidance, Control, and Dynamics, **40** (8), 1837–1859.

59 Alfriend, T.K., Vadali, S., Gurfil, P., How, J., and Breger, L. (2010) *Spacecraft Formation Flying: Dynamics, Control, and Navigation*, Elsevier Astrodynamics Series.

60 Schaub, H. and Junkins, J.L. (2003) *Analytical Mechanics of Space Systems*, AIAA.

61 Setty, S., Cefola, P., Montenbruck, O., and Fiedler, H. (2013) Investigating the suitability of analytical and semi-analytical satellite theories for space object catalogue maintenance in geosynchronous regime, in *Proceedings of AAS/AIAA Astrodynamics Specialist Conference*, Hilton Head, South Carolina.

62 Tschauner, J. and Hempel, P. (1964) Optimale beschleunigungsprogramme fuer das rendezvous-manoever. *Astronautica Acta*, **10** (3), 296–307.

63 Koenig, A., Guffanti, T., and D'Amico, S. (2017) New state transition matrices for spacecraft relative motion in perturbed orbits. *Journal of Guidance, Control, and Dynamics*, **40** (7), 1749–1768.

64 Brouwer, D. (1959) Solution of the problem of artificial satellite theory without drag. *Astronomical Journal*, **64**, 378.

65 Guffanti, T., D'Amico, S., and Lavagna, M. (2017) Long-term analytical propagation of satellite relative motion in perturbed orbits, in *Proceedings of 27th AAS/AIAA Space Flight Mechanics Meeting*, San Antonio, Texas.

66 Carpenter, J.R. and Alfriend, K.T. (2006) Navigation accuracy guidelines for orbital formation flying. *Journal of the Astronautical Sciences*, **53** (2), 207–219.

67 Carpenter, J.R. and Schiesser, E.R. (2001) Semimajor axis knowledge and gps orbit determination. *NAVIGATION: Journal of The Institute of Navigation*, **48** (1), 57–68. Also appears as AAS Paper 99–190.

68 How, J.P., Breger, L.S., Mitchell, M., Alfriend, K.T., and Carpenter, R. (2007) Differential semimajor axis estimation performance using carrier-phase differential global positioning system measurements. *Journal of Guidance, Control, and Dynamics*, **30** (2), 301–313.

69 Zhu, S., Reigber, C., and Koenig, R. (2004) Integrated adjustment of champ, grace, and gps data. *J Geodesy*, **78** (2), 103–108.

70 Laurichesse, D., Mercier, F., Berthias, J., Broca, P., and Cerri, L. (2009) Integer ambiguity resolution on undifferenced gps phase measurements and its application to ppp and satellite precise orbit determination. *Navigation J ION*, **56** (2), 135–149.

71 McGee, L.A. and Schmidt, S.F. (1985) Discovery of the kalman filter as a practical tool for aerospace and industry, *Tech. Rep. 86847*, NASA Ames Research Center.

72 Ilyas, M., Lim, J., Lee, J., and Park, C. (2008) Federated unscented kalman filter design for multiple satellites formation-flying in leo, in *Proceedings of the International Conference on Control, Automation, and Systems*, Seoul, Korea.

73 Julier, S. and Uhlmann, J. (2004) Unscented filtering and nonlinear estimation. *IEEE Trans Autom Contr*, **92** (3), 401–422.

74 Zanetti, R., DeMars, K.J., and Bishop, R.H. (2010) Underweighting nonlinear measurements. *Journal of Guidance, Control and Dynamics*, **33** (5), 1670–1675.

75 Bierman, G.J. (1977) *Factorization Methods for Discrete Sequential Estimation*, Academic Press, New York.

76 Carpenter, R. and Lee, T. (2008) A stable clock error model using coupled first- and second-order gauss-markov processes, in *AAS/AIAA 18th Spaceflight Mechanics Meeting*, vol. 130, Univelt, pp. 151–162.

77 Schmidt, S.F. (1966) *Advances in Control Systems*, Academic Press, vol. 3, chap. Applications of State Space Methods to Navigation Problems, pp. 293–340.

78 Ardaens, J. and Fischer, D. (2011) Tandem-x autonomous formation flying system: Flight results, in *Proceedings of the 18th IFAC World Congress*, Milan, Italy.

79 Winternitz, L.B., Bamford, W.A., and Price, S.R. (2017) New high-altitude gps navigation results from the magnetospheric multiscale spacecraft and simulations at lunar distances, in *Proceedings of ION GNSS+ 2017*, Portland, Oregon.

80 Farahmand, M., Long, A., Hollister, J., Rose, J., and Godine, D. (2017) Magnetospheric multiscale mission navigation performance during apogee-raising and beyond, in *Proceedings of the AAS*.